Blunt-body paradox and transient growth on a hypersonic spherical forebody

Pedro Paredes, Meelan M. Choudhari, and Fei Li

Phys. Rev. Fluids **2**, 053903 — Published 24 May 2017

DOI: 10.1103/PhysRevFluids.2.053903

On blunt-body paradox and transient growth on a hypersonic spherical forebody

Pedro Paredes,* Meelan M. Choudhari, and Fei Li

Computational AeroSciences Branch,

NASA Langley Research Center, Hampton, VA 23681, USA

(Dated: May 3, 2017)

Abstract

Roughness-induced transient growth has emerged as a possible cause for transition in linearly-stable boundary layer flows over spherical forebodies. This paper investigates the optimal growth of perturbations in the axisymmetric, laminar boundary layer over a hemisphere placed in a Mach 7.32 free stream, with the goals of contributing further insights and revisiting highly successful, transient-growth based prediction criteria for subcritical transition over blunt body configurations. Earlier predictions based on local-similarity approximation to the basic state are extended to a basic state that is obtained from the compressible Navier-Stokes equations, and hence, accounts for the presence of the bow shock, the nonsimilar development of the boundary layer, and the convex curvature of the body surface. The predicted transient growth characteristics are profoundly different from the previous body of results for boundary layer flows over flat plates and circular cones. More importantly, the selections of energy norm and objective function used to compute optimal growth exert a crucial influence on the optimal growth characteristics of a blunt body. With the conventional energy norm based on both kinetic and thermodynamic fluctuations, the highest energy gain from the input station to the output station occurs over relatively short optimization intervals in the vicinity of the stagnation point; however, the associated kinetic energy gain, which is more closely linked to transition via streak instabilities, is rather small in magnitude. On the other hand, the mean kinetic energy gain is maximized when the disturbance inflow location nearly coincides with the location corresponding to peak wall shear associated with the basic state. Assuming that the roughness-induced disturbance velocities are proportional to the roughness height, the maximum disturbance kinetic energy would be reached in the vicinity of the sonic point, which could explain the measured onset of transition within this region during prior wind-tunnel and flight experiments.

* pedro.paredes@nasa.gov

I. INTRODUCTION

The most common approach to transition prediction relies on modal growth, i.e., exponential amplification of discrete eigensolutions. The classical linear stability theory is mainly concerned with individual sinusoidal waves propagating in the boundary layer adjacent to the wall. The stability characteristics are often evaluated by using the quasiparallel approximation that reduces the linearized equations of fluid motion to an eigenvalue problem based on ordinary differential equations. In the limit of incompressible flows, this eigenvalue problem corresponds to a combination of the Orr-Sommerfeld and Squire equations [1, 2]. Effects of weak boundary layer growth, i.e., mean-flow nonparallelism can be accounted for by using multiple-scales theory (or other similar approaches) [3], which yields the leading order correction to the local amplification rate and phase speed predicted by the quasiparallel theory. A more useful extension to the nonparallel stability theory was proposed by Herbert [4], who introduced the concept of Parabolized Stability Equations (PSE). The main advantages of the PSE technique with respect to the local multiple-scales approach include its improved computational efficiency and the possibility of accounting for nonlinear interactions [5]. Since then, the PSE technique has been applied to a variety of problems, including the linear and nonlinear evolution of instability waves in 2D and 3D shear flows across a broad range of speeds.

Besides the exponential growth characteristics of convectively unstable eigenmodes in a boundary layer flow, external disturbances, e.g., freestream turbulence and surface roughness, can also have a large influence on the transition process. An additional route to transition may involve nonmodal growth, which refers to situations in which transient algebraic growth of disturbance energy is observed even when the flow is modally stable, i.e., all eigenmodes are damped. Mathematically, the transient growth is associated with the nonorthogonality of the eigenvectors corresponding to the linear disturbance equations. Physically, the main growth mechanism corresponds to the lift-up effect [6–8], which results from the conservation of horizontal momentum in the course of spanwise varying wall-normal displacement of the fluid particles. Schmid and Henningson [2] and Schmid [9] provide a thorough review of transient growth theory and results.

Recently, transient growth has been suggested as a candidate mechanism for many cases of bypass transition [10]. The term "bypass transition" has been historically used to dif-

ferentiate the well known paths to transition via modal amplification of small-amplitude disturbances from the transition phenomena that are not fully understood on a theoretical basis [11, 12]. Examples of bypass transition are the transition due to high levels of free-stream disturbances, as for example in turbomachinery, or the subcritical transition observed in Poiseuille pipe flow experiments [13–16], transition due to distributed surface roughness on flat plates [17, 18] or cones [19], and subcritical transition observed on spherical forebodies [20–26].

The present study focuses on the subcritical, bypass transition observed on spherical forebodies at hypersonic speeds. The boundary layer flow over a blunt body, e.g., a reentry capsule, does not support the growth of modal instability waves. Tollmien-Schlichting waves are stable because of the strong favorable pressure gradient. The convex curvature of the geometry prevents the growth of Görtler disturbances. Furthermore, the crossflow velocity component of the boundary layer is small for spherical shapes, which excludes the appearance of crossflow instabilities. However, several experimental measurements at different flow conditions have demonstrated that transition does occur [20, 23, 26]. This problem has been denominated the "blunt-body paradox." [21]. The distinction between subcritical and supercritical roughness conditions is important because, in the limit of supercritical conditions, i.e., large roughness elements, the modification of the mean flow by the roughness elements is such that the flow can become globally unstable and transition occurs very close to the roughness location [27–33]. For the subcritical conditions assumed in the present study, empirical transition correlations [28, 34–36] have shown a good agreement with experimental measurements under the assumption that the receptivity of stationary disturbances to distributed roughness is linear with the peak-to-valley height k, i.e., the initial amplitude of the induced disturbance is proportional to k. The stationary disturbances induced by discrete roughness elements are significantly different in shape from the theoretical optimum, yet they can experience significant nonmodal growth depending on the roughness characteristics [37–42].

As a result of the blunt-body paradox, transition onset over reentry vehicle nose tips is commonly predicted via empirical transition correlations. One such well-known correlation is based on the extensive set of measurements carried out under the PAssive Nosetip Technology (PANT) Program [43, 44]. In its original form, the PANT correlation was expressed

as

$$Re_\Theta \left(\frac{k}{\Theta}\frac{T_e}{T_w}\right)^{0.7} = \begin{cases} 255 \text{ at } M_e = 1: & \text{transition onset,} \\ 215: & \text{onset location,} \end{cases} \tag{1}$$

where Re_Θ is the boundary layer momentum thickness Reynolds number, Θ is the momentum thickness, T_e is the edge temperature, T_w is the wall temperature, and M_e is the edge Mach number. In the PANT data, transition was usually observed to occur upstream of the sonic point. The PANT correlation for transition onset is based on the observation that transition onset only occurred in cases where the transition parameter on the left hand side of Eq. (1) exceeded a value of 255 at the sonic point and the onset location itself correlated with the position where this parameter equaled 215. The PANT correlation was examined by Reda and Leverance [34] and Reda [35] for actual conditions of reentry environment as simulated in a ballistic range. Significant discrepancies were noted between predicted and experimentally observed transition zone behavior. By using the same form of Eq. (1), a modified correlation was obtained through a curve fitting of the ballistic range data,

$$Re_\Theta \left(\frac{k}{\Theta}\frac{T_e}{T_w}\right)^{1.30} = 574. \tag{2}$$

Recently, Reshotko and Tumin [36] developed a transition correlation based on "parallel" transient growth results for self-similar axisymmetric stagnation point flow. Such parallel transient growth analysis does not account for the downstream evolution of the boundary layer and the geometry variation, because it assumes a spatially invariant base flow profile at every streamwise station. Their correlation for the PANT wind-tunnel database, which was also shown to correlate well with Reda's ballistic-range data, was

$$Re_\Theta \left(\frac{k}{\Theta}\right)\left(\frac{T_e}{T_w}\right)^{1.27} = 434. \tag{3}$$

The form of this correlation is very similar to that of Reda from Eq. (2), with the main difference being the exponent of the roughness-height parameter on the left hand side of each correlation. The transition parameter in the Reshotko and Tumin correlation depends linearly on k/Θ, because they assumed the initial disturbance amplitude to scale linearly with the roughness-height parameter. Despite the favorable agreement between the correlation from Eq. (3) and the available experiments, the accuracy of transient growth predictions underlying Eq. (3) remains questionable because of the parallel-flow assumption together with the neglect of surface curvature effects, and secondarily, the approximations involved in basic state computations.

Spatial transient growth analysis, including nonparallel effects, of the boundary layer over a sphere at freestream Mach number of 6 was presented by Tumin and Reshotko [45] and Zuccher *et al.* [46]. In these studies, the velocity and temperature profiles were calculated using local-similarity approximation. Mack's energy norm [47], which accounts for kinetic and thermodynamic fluctuations as explained in Section II, was used to measure the growth of the optimal initial perturbations. Their results showed that the optimal energy amplification is stronger in the vicinity of the stagnation point and for short optimization intervals; however, the optimal optimization intervals were not reported. Also, the streamwise convex curvature was found to reduce transient growth. The results do not appear to explain the experimental observation, that, when the roughness height is increased, the transition location was first observed in the vicinity of the sonic point and then moved upstream up to a certain distance from the stagnation point [23, 26, 44].

The nonparallel spatial transient growth analysis in the present paper is based on the compressible Navier-Stokes (NS) computations [48] of laminar flow over a hemisphere of radius $R = 0.0889$ m at zero angle of attack. The freestream conditions are selected to match the experiments by Kaattari [49], namely, $M_\infty = 7.32$, $Re' = 14.6 \times 10^6$ /m, and $T_\infty = 65$ K, and isothermal wall condition with $T_w = 300$ K. Recently, Li *et al.* [48] examined the effects of outgassing on the modal instability of boundary layer flow over this body and found the modal growth to be insignificant in the absence of any outgassing. The mass-injection rate was defined as $\mu_{in} = \rho_w v_w/(\rho_\infty u_\infty)$, where ρ_w and v_w denote the density and velocity normal to the wall, respectively, of the injected fluid, and the subscript ∞ denotes freestream values. First mode waves were observed to become marginally unstable for $\mu_{in} \approx 0.007$, which is a value larger than those corresponding to typical injection rates. The mass-injection rate needed to reach N-factor values of $N = 7$ to $N = 13$ were $\mu_{in} = 0.01$ to $\mu_{in} = 0.013$, respectively. Therefore, transition in zero or weak outgassing cases presents yet another example of the blunt-body paradox. For the selected flow conditions, Kaattari [49] experimentally studied the effect of mass injection on wall heat transfer. He observed that, upon mass injection, the onset of transition begins a few degrees downstream of the sonic point and moves upstream as the mass injection is increased.

The present transient growth analysis includes two separate definitions of the objective function or energy gain; namely, the ratio between the energy norm at the outlet and inlet locations, which was used by Refs. [45, 46], and the ratio between the mean energy norm

along the optimization interval and the energy at the inlet location, which accounts for possible overshoots in energy evolution across the optimization range. Furthermore, two different energy norm definitions are selected. Besides the conventional energy norm used for compressible boundary layer flows that includes kinetic and thermodynamic fluctuations developed by Mack [47], the kinetic energy alone is also used as the energy norm. The reason to look at the kinetic energy growth is the finding from the stability analysis of finite-amplitude streaks in compressible boundary layers [50, 51] where the secondary instabilities that would lead to bypass transition are driven by the strength of the streamwise velocity shear of the streak. Therefore, secondary instabilities are expected to become unstable when the transient growth is able to produce a disturbance with higher kinetic energy. Paredes *et al.* [52] presented the nonlinear evolution of finite-amplitude optimal perturbations and the instability analysis of the resulting streaks. Their results show that the boundary layer perturbed by finite-amplitude streaks becomes unstable for streak amplitudes of $As_u > 0.16$, where $As_u(\xi) = [\max_{\eta,\zeta}(\tilde{u}) - \min_{\eta,\zeta}(\tilde{u})]/(2\bar{u}_\infty)$.

We note that the optimal growth theory does not address the generation (i.e., receptivity) of streak disturbances responsible for bypass transition; and, in fact, disturbance profiles resulting from realistic external disturbances usually result in suboptimal transient growth [40, 53, 54]. While this represents a clear limitation of the optimal growth theory, it does contribute useful insights by providing an upper bound on the nonmodal energy amplification due to spanwise periodic disturbances. Indeed, for reasons that are not fully understood as yet, transition correlations derived from optimal growth considerations appear to capture the measured trends related to blunt-body paradox, as mentioned in the context of Eq. (3). The present work may be viewed as an initial step toward the assessment and potential improvement of such correlations, by extending the application of spatial transient growth to nonsimilar flows.

The paper is organized as follows. Section II provides a summary of the optimal growth theory based on the PSE. The results are presented in Section III that is subdivided into three subsections. The characteristics of the laminar flow over the hemisphere are presented in Subsection III A, together with the application of previous transition correlations to the computed basic state. Transient growth results for the hypersonic spherical forebody are presented in Subsection III B, including the comparison of predictions based on two separate energy gain definitions; namely, the ratio between outlet and inlet disturbance energy norms

and the ratio between mean and inlet disturbance energy norms. Also, results are obtained for the optimization of the Mack's energy norm that accounts for kinetic and thermodynamic fluctuations and for optimization of the kinetic energy alone. In Subsection III C, the implications of the transient growth predictions are investigated, especially in the context of the correlations for roughness-induced transition and the experimental measurements by Kaattari [49]. Conclusions are presented in Section IV.

II. METHODOLOGY

Transient growth analysis is performed using the linear PSE as explained in the literature [55–58]. For completeness, the present section outlines the methodology, which bears strong similarities with the optimization approach based on the linearized boundary layer equations [59–61]. The advantage of the PSE-based formulation is that it is also applicable to more complex base flows where the flow evolves along the streamwise direction and the boundary layer approximation may not hold. The PSE approach can also be easily extended to unsteady disturbances. While infinite Reynolds number asymptotic results cannot be directly computed using this technique, good agreement is achieved between the two methodologies for incompressible and compressible regimes as shown by Paredes *et al.* [58, 62].

In the PSE context, the perturbations have the form

$$\tilde{\mathbf{q}}(\xi,\eta,\zeta,t) = \hat{\mathbf{q}}(\xi,\eta)\exp\left[\mathrm{i}\left(\int_{\xi_0}^{\xi}\alpha(\xi')\,\mathrm{d}\xi' + \beta\zeta - \omega t\right)\right] + \text{c.c.}, \tag{4}$$

where c.c. denotes complex conjugate. The suitably nondimensionalized, orthogonal, curvilinear coordinate system (ξ,η,ζ) denotes streamwise, wall-normal, and spanwise coordinates and (u,v,w) represent the corresponding velocity components. Density and temperature are denoted by ρ and T. The Cartesian coordinates are represented by (x,y,z). The vector of perturbation fluid variables is $\tilde{\mathbf{q}}(\xi,\eta,\zeta,t) = (\tilde{\rho},\tilde{u},\tilde{v},\tilde{w},\tilde{T})^T$ and the vector of amplitude functions is $\hat{\mathbf{q}}(\xi,\eta) = (\hat{\rho},\hat{u},\hat{v},\hat{w},\hat{T})^T$. The vector of basic state variables is $\bar{\mathbf{q}}(\xi,\eta) = (\bar{\rho},\bar{u},\bar{v},\bar{w},\bar{T})^T$. The streamwise and spanwise wavenumbers are α and β, respectively; and ω is the angular frequency of the perturbation.

Upon introduction of the perturbation form (4) into the linearized NS equations together with the assumption of a slow streamwise dependence of the basic state and the amplitude

functions, thus neglecting the viscous derivatives in ξ, the PSE are recovered as follows

$$\mathbf{L}\hat{\mathbf{q}}(\xi,\eta) = \left(\mathbf{A} + \mathbf{B}\frac{\partial}{\partial\eta} + \mathbf{C}\frac{\partial^2}{\partial\eta^2} + \mathbf{D}\frac{1}{h_\xi}\frac{\partial}{\partial\xi}\right)\hat{\mathbf{q}}(\xi,\eta) = 0. \tag{5}$$

The linear operators $\mathbf{A}$, $\mathbf{B}$, $\mathbf{C}$ and $\mathbf{D}$ are given by Pralits *et al.* [55] and h_ξ is the metric factor associated with the streamwise curvature. The system of Eqs. (5) is not fully parabolic due to the term $\partial\hat{p}/\partial\xi$ in the streamwise momentum equation, and also due to the presence of other terms that are quadratic in the streamwise wavenumber α [63–66]. However, for the purely stationary disturbances of interest in this work, $\alpha = 0$ and the pressure gradient term $\partial\hat{p}/\partial\xi$ can be dropped from the equations as justified by Refs. [56, 67], which found that $\partial\hat{p}/\partial\xi$ is of higher order for transient growth problems, and, therefore, can be neglected without any significant loss of accuracy.

The optimal initial disturbance, $\tilde{\mathbf{q}}_0$, is defined as the initial (i.e., inflow) condition at ξ_0 that maximizes the objective function, J, which is defined as a measure of disturbance growth over a specified interval $[\xi_0, \xi_1]$. The definitions used in the present study correspond to the outlet energy gain $J = G^{out}$ and mean energy gain $J = G^{mean}$ and are defined as

$$G^{out} = \frac{E(\xi_1)}{E(\xi_0)}, \tag{6}$$

$$G^{mean} = \frac{1}{\xi_1 - \xi_0}\frac{\int_{\xi_0}^{\xi_1} E(\xi')\,d\xi'}{E(\xi_0)}, \tag{7}$$

where E denotes the energy norm of $\tilde{\mathbf{q}}$. The energy norm is defined as

$$E(\xi) = \int_\eta \hat{\mathbf{q}}(\xi,\eta)^H \mathbf{M}_E \hat{\mathbf{q}}(\xi,\eta)\, h_\xi\, h_\zeta\, \mathrm{d}\eta, \tag{8}$$

where h_ζ is the metric factor associated with the azimuthal curvature, $\mathbf{M}_E$ is the energy weight matrix and the superscript H denotes conjugate transpose. The selection of G^{out} corresponds to the "outlet energy gain" that is commonly used in studies of the optimal-perturbation problem [59, 60]. The selection of G^{mean} defines the "mean energy gain" and corresponds to the optimization of the mean energy. This latter definition accounts for a possible overshoot in the disturbance energy evolution that are not accounted for by the former definition and is found to be present in the hemisphere case as documented in Subsection III B.

The choice of the energy norm is known to influence the optimal initial perturbation as well as the magnitude of energy amplification [46, 57, 61]. Here, we use the positive-definite

energy norm derived by Mack [47] and Hanifi *et al.* [68], which is defined by

$$\mathbf{M}_E = \mathrm{diag}\left[\frac{\bar{T}(\xi,\eta)}{\gamma\bar{\rho}(\xi,\eta)M^2}, \bar{\rho}(\xi,\eta), \bar{\rho}(\xi,\eta), \bar{\rho}(\xi,\eta), \frac{\bar{\rho}(\xi,\eta)}{\gamma(\gamma-1)\bar{T}(\xi,\eta)M^2}\right]. \tag{9}$$

Additionally, the kinetic energy norm is also used for optimization in this paper. The kinetic energy of a perturbation is defined by

$$K(\xi) = \int_\eta \hat{\mathbf{q}}(\xi,\eta)^H \mathbf{M}_K \hat{\mathbf{q}}(\xi,\eta)\, h_\xi\, h_\zeta\, \mathrm{d}\eta, \tag{10}$$

where

$$\mathbf{M}_K = \mathrm{diag}\left[0, \bar{\rho}(\xi,\eta), \bar{\rho}(\xi,\eta), \bar{\rho}(\xi,\eta), 0\right]. \tag{11}$$

To differentiate when the total energy norm E or the kinetic energy norm K are used, a corresponding subscript is added to the energy gain, resulting in four options for the objective function; namely, G_E^{out}, G_E^{mean}, G_K^{out}, and G_K^{mean}.

The variational formulation of the problem to determine the maximum of the objective functional J of Eq. (7) leads to an optimality system [58], which is solved in an iterative manner, starting from a random solution at ξ_0 that must satisfy the boundary conditions. The PSE, $\mathbf{L}\tilde{\mathbf{q}} = 0$, are used to integrate $\tilde{\mathbf{q}}$ up to ξ_1, where the final optimality condition is used to obtain the initial condition for the backward adjoint PSE integration, $\mathbf{L}^\dagger\tilde{\mathbf{q}}^\dagger = c_{mean}F(\tilde{\mathbf{q}})$, where $c_{mean} = 0$ for the outlet energy gain optimization and $c_{mean} = 1$ for the mean energy gain optimization, and $F(\tilde{\mathbf{q}})$ is a function of the direct solution [55]. At ξ_0, the adjoint solution is used to calculate the new initial condition for the forward PSE integration with the initial optimality condition. The iterative procedure finishes when the value of J has converged up to a certain tolerance, which was set to 10^{-4} in the present computations.

Nonuniform stable high-order finite difference schemes (FD-q) [69, 70] of sixth order are used for discretization of the PSE along the wall-normal coordinate. The discretized PSE are integrated along the streamwise coordinate by using second-order backward differentiation. The number of discretization points in both directions was varied in selected cases to ensure convergence of the optimal gain predictions. The wall-normal direction was discretized using $N_y = 201$, with the nodes being clustered toward the wall [70]. No-slip, isothermal boundary conditions are used at the wall, i.e., $\hat{u} = \hat{v} = \hat{w} = \hat{T} = 0$. The amplitude functions are forced to decay at the farfield boundary by imposing the Dirichlet conditions $\hat{\rho} = \hat{u} = \hat{w} = \hat{T} = 0$, unless otherwise stated. The farfield boundary coordinate is set just below the shock layer. Verification of the present optimal growth module against available transient growth results from the literature is shown in Refs. [58, 62].

III. RESULTS

Transient growth results are presented for the hypersonic flow over an spherical forebody. Firstly, the characteristics of the basic state are analyzed and transition correlation formulas are applied to the computed basic state solution. Then, the transient growth analysis is shown, including results for selected objective function definitions. Finally, the implications of the transient growth predictions are investigated.

A. Basic state and transition correlations

Transient growth analysis is performed for a Mach 7.32 flow over a blunt, hemispherical capsule at zero angle of attack. The freestream unit Reynolds number is $Re' = 14.6 \times 10^6$ /m, the freestream temperature is $T_\infty = 65$ K, and the total pressure $p_t = 5.5208 \times 10^6$ Pa (800 psi). The isothermal wall condition is set with $T_w = 300$ K. The radius of the body is $R = 0.0889$ m. This flow configuration corresponds to one of the conditions from the experiments presented by Kaattari [49]. The basic state boundary-layer flow over the hemisphere surface was computed on various grids by using a second-order accurate algorithm as implemented in the finite-volume compressible Navier-Stokes flow solver VULCAN-CFD (see Ref. [71] and `http://vulcan-cfd.larc.nasa.gov` for further information about the solver). Details about the numerical solution, together with the boundary conditions, and the convergence study for the basic state are given by Ref. [48]. Specifically, the code uses an iterative shock capturing adaptation of the grid and outflow nonreflective boundary conditions based on the characteristics. Here, we use the solution obtained using 258 points along the hemisphere surface and 706 points in the wall normal direction with at least 200 points in the boundary layer. The Mach number contours are shown in Fig. 1(a). The boundary-layer edge Mach number is subsonic over a significant portion of the body length and the maximum edge Mach numbers within the peripheral region are low supersonic at most.

The computational coordinates, (ξ, η, ζ), are defined as an orthogonal body-fitted coordinate system. The metric factors are defined as

$$h_\xi = 1 + \kappa\eta, \tag{12}$$

$$h_\zeta = r_b + \eta\cos(\phi), \tag{13}$$

where κ denotes the streamwise curvature, r_b is the local radius, and ϕ denotes the inclination

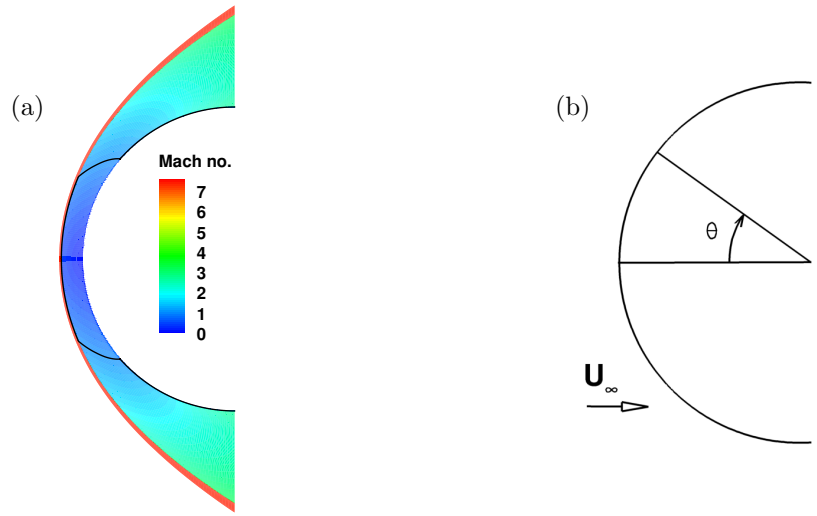

FIG. 1. (a) Mach number contours of the basic state with sonic line in black color and (b) graphical definition of angular coordinate, θ.

of the local tangent to the body surface, i.e., $\sin(\phi) = dr_b/d\xi$. The angular coordinate, θ, is related to the streamwise coordinate by $\xi = \theta\, R$. Figure 1(b) shows a graphical definition of the angular coordinate. The streamwise curvature is constant along the hemisphere, $\kappa = 1/R = 11.249$ /m, and the local radius is $r_b = R\sin(\theta)$. Note that the spanwise wavenumber β of Eq. (4) corresponds to a nondimensional, integer azimuthal wavenumber, denoted by m. In what follows, the flow variables are nondimensionalized with freestream values.

The streamwise evolution of basic state streamwise velocity $\bar{u}$, streamwise mass flux $\bar{\rho}\bar{u}$, convective momentum flux $\bar{\rho}\bar{u}^2$, temperature $\bar{T}$, and Mach number M, at the boundary-layer edge is plotted in Fig. 2(a). The boundary-layer edge, $\eta_e = \delta_h$, is defined as the wall-normal position where $h_0/h_{0,\infty} = 0.995$, where h_0 is the stagnation enthalpy. The edge streamwise velocity and edge temperature exhibit a monotonic growth and decay, respectively, with distance from the stagnation point. In agreement with inviscid flow theory, the streamwise mass-flux peak is located at the sonic point, $M_e = 1$, which is located at $\theta = 41.1°$. The peak of the convective momentum flux at boundary-layer edge $\bar{\rho}_e\bar{u}_e^2$ occurs approximately 15° downstream of the sonic point. The boundary layer thickness δ_h, the momentum thickness Θ and the boundary layer momentum-thickness Reynolds number $Re_\Theta = \bar{\rho}_e\bar{u}_e\Theta/\bar{\mu}_e$, are plotted in Fig. 2(b). The momentum thickness is roughly 10 times smaller than the boundary layer thickness δ_h.

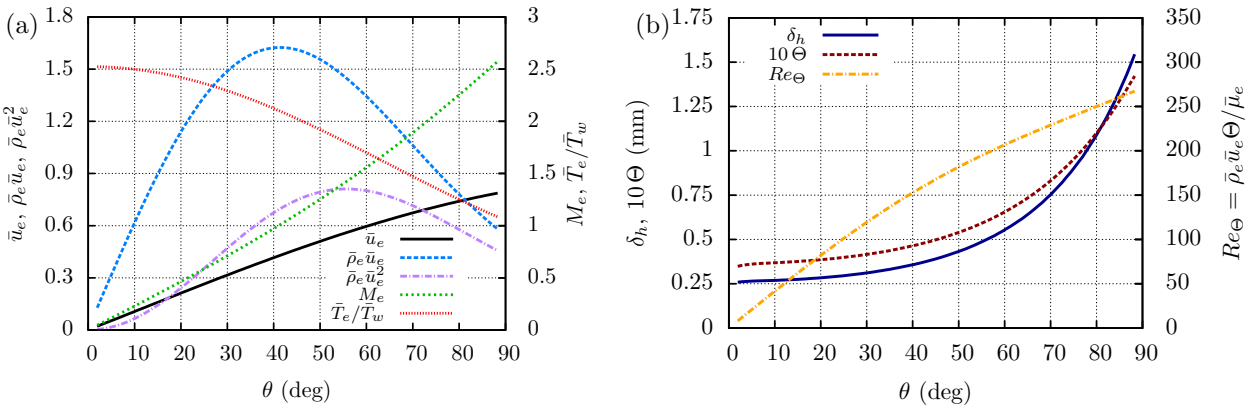

FIG. 2. Streamwise evolution of (a) basic flow variables at the edge of the boundary layer ($\bar{u}_e$, $\bar{\rho}_e\bar{u}_e$, $\bar{T}_e$, and M_e), and (b) boundary layer thickness, δ_h, boundary layer momentum thickness, Θ and boundary layer momentum thickness Reynolds number Re_Θ.

The wall shear $\tau_w = (\bar{\mu}\bar{u}_\eta)_w$ and wall heat ratio $q_w = (\bar{\kappa}\bar{T}_\eta)_w$ are proportional to the wall-normal derivative of streamwise velocity ($\bar{u}_\eta \equiv \partial\bar{u}/\partial\eta$) and temperature ($\bar{T}_\eta \equiv \partial\bar{T}/\partial\eta$) at the wall, respectively, for the present flow configuration with constant wall temperature. Both quantities, $(\bar{u}_\eta)_w$ and $(\bar{T}_\eta)_w$, are plotted in Fig. 3(a). The wall shear distribution peaks roughly 5° downstream of the sonic point. The wall heat flux monotonically decreases from the stagnation point. Figure 3(b) shows the pressure gradient parameter in terms of boundary layer scales, $\bar{\rho}_e\Theta^2/\bar{\mu}_e \times d\bar{u}_e/d\xi$. Although not shown, the pressure gradient expressed as the Hartree parameter β_H remains within 4% of the theoretical value ($\beta_H = 0.5$) up to $\theta < 30°$, but increases thereafter, reaching $\beta_H = 0.83$ at $\theta = 85°$.

The profiles of the basic state variables are plotted in Fig. 4 for $\theta = 10°$, $30°$, $60°$, and $90°$. At the locations closer to the stagnation point ($\theta = 10°$ and $30°$), the basic state velocity profiles resemble those of the classical similarity solution for stagnation point flow. Specifically, the wall-normal velocity is negative throughout the boundary layer, the streamwise velocity increases with distance from the stagnation point, and the boundary layer thickness remains nearly constant. At farther downstream locations ($\theta = 60°$ and $90°$), the wall-normal velocity becomes positive and the boundary layer thickness increases with θ. The local-similarity solution used by Refs. [45, 46] assumes a constant boundary layer thickness, a linear acceleration of the streamwise velocity, and an unaltered negative wall-normal velocity along the body length. As seen from Figs. 2(b) and 3(b), these assumptions are clearly violated beyond the sonic point, but would also lead to appreciable quantitative

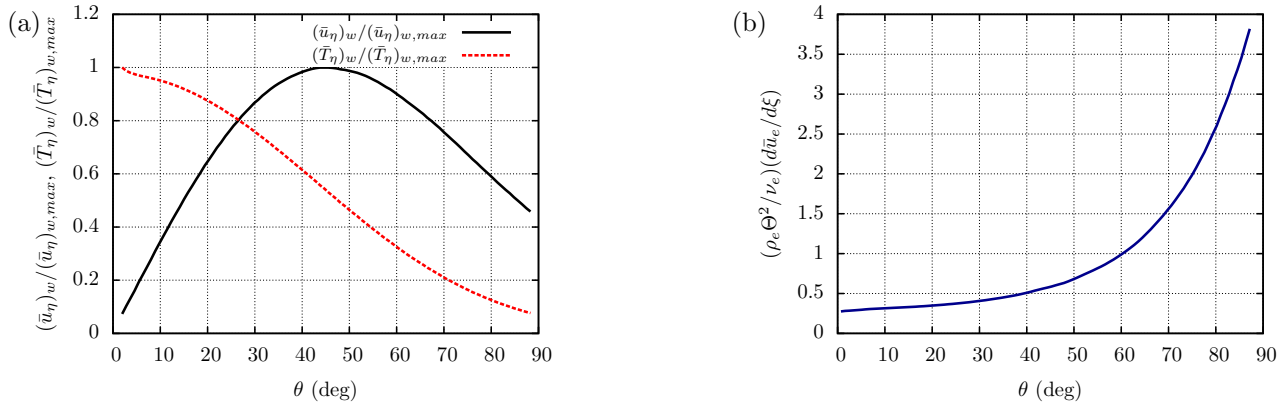

FIG. 3. Streamwise evolution of (a) wall-normal derivative of basic state streamwise velocity and temperature variables at the wall normalized with the corresponding maximum value and (b) pressure gradient parameter in terms of boundary layer scales $\bar{\rho}_e\Theta^2/\bar{\mu}_e \times d\bar{u}_e/d\xi$.

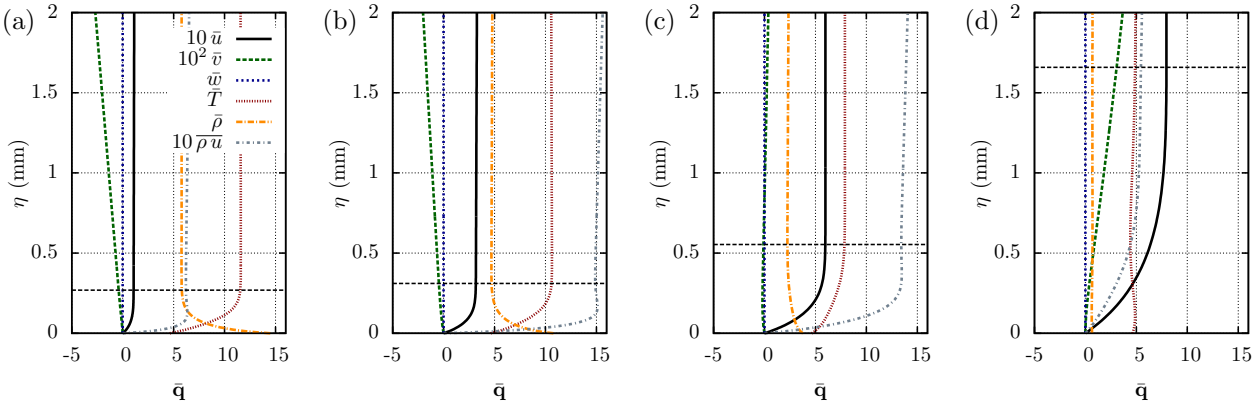

FIG. 4. Basic state variables at selected angular positions; namely, (a) $\theta = 10°$, (b) $\theta = 30°$, (c) $\theta = 60°$, and (d) $\theta = 90°$. The horizontal dashed line represents the position of the boundary-layer edge.

discrepancy up to that location.

Here, the transition correlations discussed in the Introduction are applied to the present problem. As previously mentioned, the existing transition correlations relate the value of Re_Θ at the transition onset location to a local roughness parameter, which corresponds to the nondimensional roughness height modified by a wall cooling factor, that achieves its maximum value in the vicinity of the sonic point. The PANT transition correlation from Eq. (1) assumed the empirical disturbance parameter $(\bar{T}_e/\bar{T}_w)(k/\Theta)$ to correlate with the relative kinetic energy at the top of the roughness elements, $\bar{\rho}_k\bar{u}_k^2/\bar{\rho}_e\bar{u}_e^2$. In the correlation

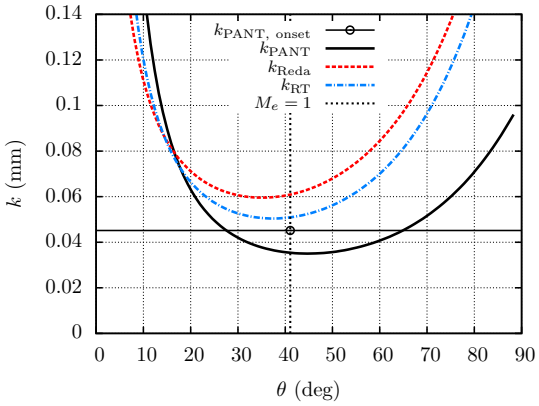

FIG. 5. Roughness heights needed for transition to occur following the PANT (k_{PANT}), Reda (k_{Reda}) and Reshotko & Tumin (k_{RT}) correlations. The vertical dotted line denotes the sonic point.

developed by Reshotko and Tumin [36], the roughness-induced energy is assumed to be proportional to the relative kinetic energy, $\bar{\rho}_k \bar{u}_k^2 / \bar{\rho}_e \bar{u}_e^2$, the roughness-induced velocities are assumed to be proportional to the roughness height, $\bar{u}_k / \bar{u}_e \propto k/\Theta$, and the wall-cooling ratio $\bar{T}_e / \bar{T}_w$ is assumed to be equal to $\bar{\rho}_k / \bar{\rho}_e$. Then, the input energy was assumed to be $E_{in} \propto (\bar{T}_e / \bar{T}_w)(k/\Theta)^2$. Furthermore, the energy norm at transition is related to this input energy through the "parallel" transient growth energy gain G, i.e., $E_{tr} = G E_{in}$. The dependence of the energy gain on the wall-cooling factor and Reynolds number was obtained with parallel transient growth computations using self-similar stagnation flow profiles. Finally, the correlation constant on the right hand side of Eq. (3) was obtained by fitting with the PANT wind-tunnel and Reda's ballistic range databases [35, 44, 72]. The roughness heights needed to meet the previously introduced boundary layer transition correlations for the present configuration of a hemispherical forebody are plotted in Fig. 5 as a function of the angular position. The roughness height needed for transition to occur as predicted by the three correlations falls within the narrow range of $k \in (0.045, 0.060)$ mm. The three theories agree that the transition location would first occur upstream of the sonic point for a uniform roughness height along the body surface.

B. Transient growth characteristics

For a nonsimilar boundary layer such as the hemispherical forebody, both the initial and final locations must be varied in order to obtain an overall picture of the optimal growth characteristics. Thus, the computational effort involved is significantly greater than that of a self-similar boundary layer such as a flat plate or a sharp cone. The transient growth results are subdivided in two parts. First, the effect of inflow and outflow disturbance locations, azimuthal wavenumber, and streamwise and azimuthal curvatures, as well as the definition of the objective function corresponding to either outlet or mean energy gain definitions are studied. Secondly, the overall results are presented for the mean total and kinetic energy gains.

1. Effect of disturbance parameters and objective function definitions

First, we consider transient growth results based on the commonly used energy norm E of Eq. (8), which accounts for both kinetic and thermodynamic fluctuations. Figures 6(a) through 6(d) illustrate the effect of initial disturbance location θ_0 and azimuthal wavenumber m on the optimal outlet energy gain G_E^{out} at a fixed output location. Four different outflow locations are chosen to cover a majority of the computational domain. They vary from a location shortly downstream of the stagnation point ($\theta_1 = 12.9°$) to the outflow of the computational domain ($\theta = 90°$). For each of these outflow locations, several inflow locations are chosen to help illustrate the overall trends in transient growth characteristics, which are plotted in Fig. 6, for each of these optimization intervals (θ_0, θ_1). Results for the farthest downstream outlet location ($\theta_1 = 90.0°$) are shown in Fig. 6(a), whereas Fig. 6(d) displays the results for an output location that is modestly downstream of the stagnation point ($\theta_1 = 12.9°$). As shown in previous studies using self-similar boundary layer profiles over a sphere [45, 46], the energy amplification is stronger for outflow locations closer to the stagnation point (Fig. 6(d)). Results for $\theta_1 = 64.5°$ and $\theta_1 = 90.0°$ show a larger energy gain for shorter optimization intervals, i.e., when the inflow location is only modestly upstream of the outflow location, showing a maximum for $\theta_0 \approx 83.8°$ with $\theta_1 = 90.0°$ and for $\theta_0 \approx 61.2°$ with $\theta_1 = 64.5°$. Results for outflow locations closer to the stagnation point, i.e., $\theta_1 = 32.2°$ (Fig. 6(c)) and $\theta_1 = 12.9°$ (Fig. 6(d)), show a similar behavior to the transient growth results on the

incompressible, stagnation, planar Hiemenz flow [62]. For these cases, as the inflow location moves closer to the stagnation point from the inflow station corresponding to the first local maximum in Figs. 6(c) and 6(d) ($\theta_0 \leq 16.1^\circ$ for $\theta_1 = 32.2^\circ$ and $\theta_0 \leq 7.73^\circ$ for $\theta_1 = 12.9^\circ$), the optimal gain continues to increase in a monotonic fashion. As described by Paredes *et al.* [62], this increase is accompanied by a change in the optimum initial disturbance. For initial disturbance locations close to both planar and axisymmetric stagnation points, where the basic state exhibits a strong negative wall-normal velocity relative to the streamwise velocity, the wall-normal extent of the optimal disturbance shape function becomes much longer than the thickness of the boundary layer. Figure 7(a) shows the initial and final amplitude vectors for one such case where the initial position is close to the stagnation point, specifically, $\theta_0 = 9.67^\circ$, $\theta_1 = 32.2^\circ$, and $m = 130$. Observe that the wall-normal velocity component of the perturbation extends up to the shock layer ($\eta \approx 6.7$ mm). For this case, a Neumann boundary condition was set at the far field for all the perturbation variables. As seen from Fig. 7(a), the resulting mode shapes do approach zero perturbation values in the far-field boundary. The resulting gain was nearly unaffected and the most significant impact was to allow a smooth perturbation decay outside the boundary layer up to the far-field boundary. This boundary condition was also used to obtain the optimal energy gain of Fig. 6(d) for $\theta_0 = 3.22^\circ$ and $\theta_1 = 12.9^\circ$. If the disturbance profiles were to extend even further, i.e., up to the body-shock location, then the boundary conditions will need to be modified to explicitly account for the shock [73]. However, the physical significance of the parametric region where this change becomes necessary remains open to question, especially in the context of problems where the suspected cause for transition is linked to surface roughness. The long extent of the perturbation and the associated small optimal azimuthal wavenumbers are unlikely to represent roughness-induced transition. Therefore, the present results are confined to the (entire) region of initial locations where the initial profiles are deemed to be not influenced by the shock. For the initial location corresponding to the local maximum of energy gain for short optimization intervals, i.e., $\theta_0 = 25.8^\circ$ and $m = 320$ in Fig. 6(c), Fig. 7(b) shows that the peak of the wall-normal velocity is located at $\eta \approx 0.2$ mm, and the disturbance components quickly decay to zero farther away from the surface. In contrast to the differences in optimum initial profiles depending on the value of θ_0, the final disturbance profiles for both $\theta_0 = 9.67^\circ$ (Figs. 7(a)) and $\theta_0 = 25.8^\circ$ (Figs. 7(b)) are almost identical to each other.

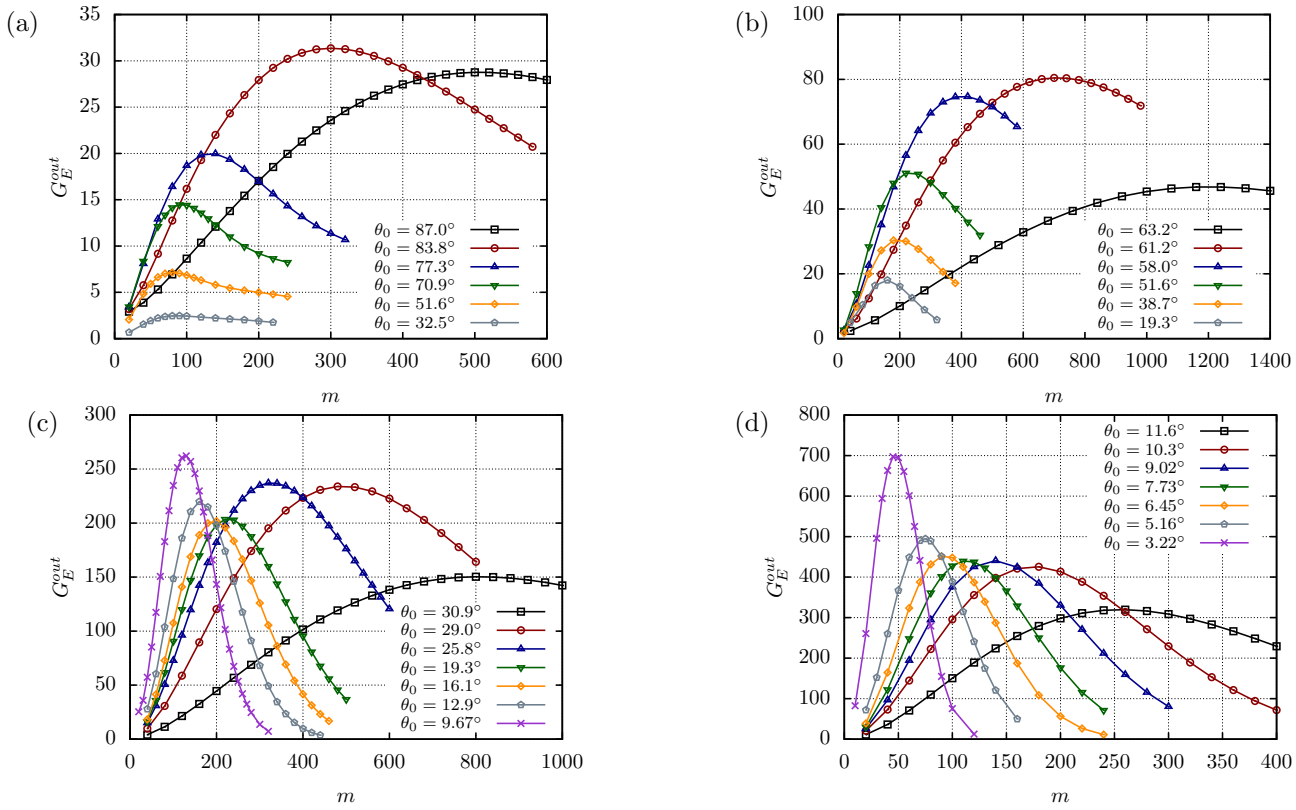

FIG. 6. Optimal outlet energy gain G_E^{out} as a function of the azimuthal wavenumber m for selected initial and final optimization positions; namely, (a) $\theta_1 = 90.0°$, (b) $\theta_1 = 64.5°$, (c) $\theta_1 = 32.2°$, and (d) $\theta_1 = 12.9°$.

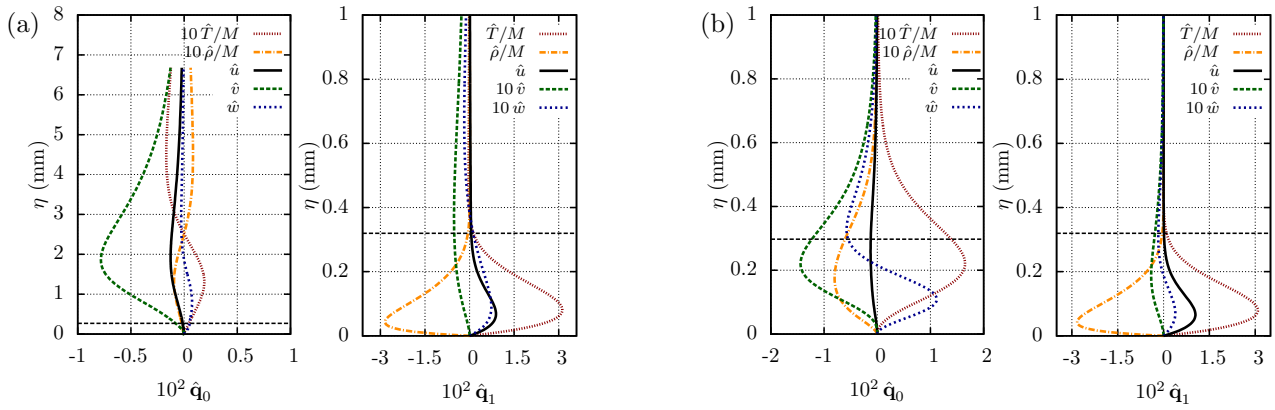

FIG. 7. Initial and final amplitude vectors for optimal outlet energy gain G_E^{out}, $\theta_1 = 32.2°$, and (a) $\theta_0 = 9.67°$ and $m = 130$ and (b) $\theta_0 = 25.8°$ and $m = 320$. The profiles are normalized with the local energy norm E. The horizontal dashed lines represent the boundary-layer edges.

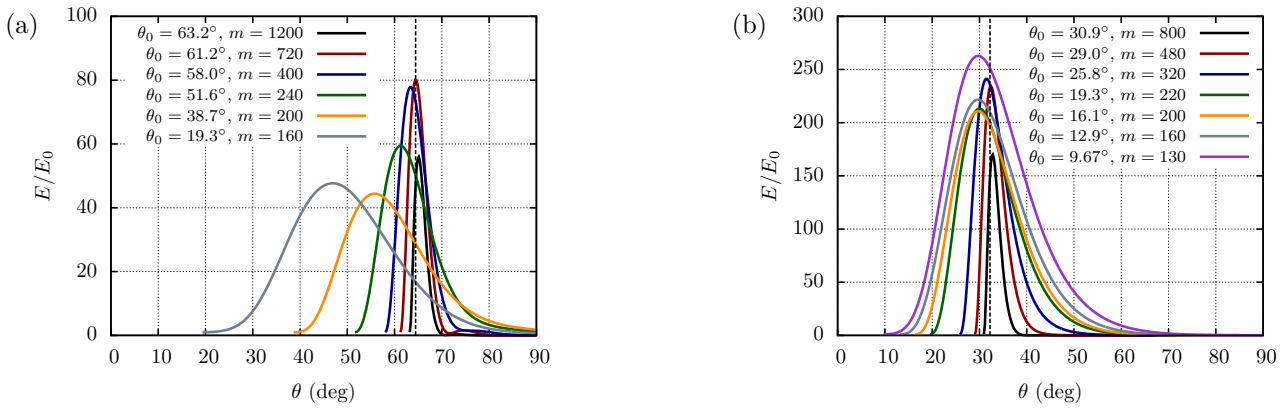

FIG. 8. Evolution of energy norm for highest outlet energy gain G_E^{out} for selected initial location for a fixed θ_1: (a) $\theta_1 = 64.5°$ and (b) $\theta_1 = 32.2°$. The plots display energy evolution over the entire length of hemisphere and the fixed value of θ_1 in each case is indicated by the vertical dashed line.

Figure 8 shows the streamwise evolution of the energy norm E for optimal outlet energy gain with optimal azimuthal wavenumbers and selected initial locations shown in Figs. 6(b) and 6(c) with $\theta_1 = 64.5°$ and $\theta_1 = 32.2°$, respectively. Although the outlet energy gain at $\theta = \theta_1$ is being optimized, the location of maximum energy norm is located within the range of optimization, i.e., at $\theta_0 < \theta < \theta_1$, instead of at the outlet location θ_1 for most of the selected initial locations. This finding is a consequence of the geometry and flow acceleration along the body. The subsequent decay in the energy norm up to $\theta = \theta_1$ indicates that the optimization of the mean energy gain G_E^{mean} might be more appropriate for this problem.

The effect of streamwise and azimuthal curvatures is studied in Fig. 9. Optimal outlet energy gains as a function of the azimuthal wavenumber for the initial and final locations of Fig. 6(b) are calculated using the same basic state profiles but by artificially setting $h_\xi = 1$ to neglect the effects of streamwise curvature (Fig. 9(a)) and $h_\zeta = 1$ to neglect the effects of azimuthal curvature (Fig. 9(b)). The comparison with results including the effect of both curvature terms (dashed lines) shows that the streamwise curvature has a stronger effect than the azimuthal curvature. As expected, the effects of the streamwise and azimuthal curvatures become stronger as the optimization interval is increased. The maximum energy gain is slightly reduced after dropping the azimuthal curvature terms, with a maximum reduction that is less than a factor of 2 for $\theta_0 = 19.3°$ in Fig. 9(b). However, neglecting the streamwise curvature terms (Fig. 9(a)) changes the transient growth behavior, reaching the maximum energy gain for a different azimuthal wavenumber and optimization interval, and

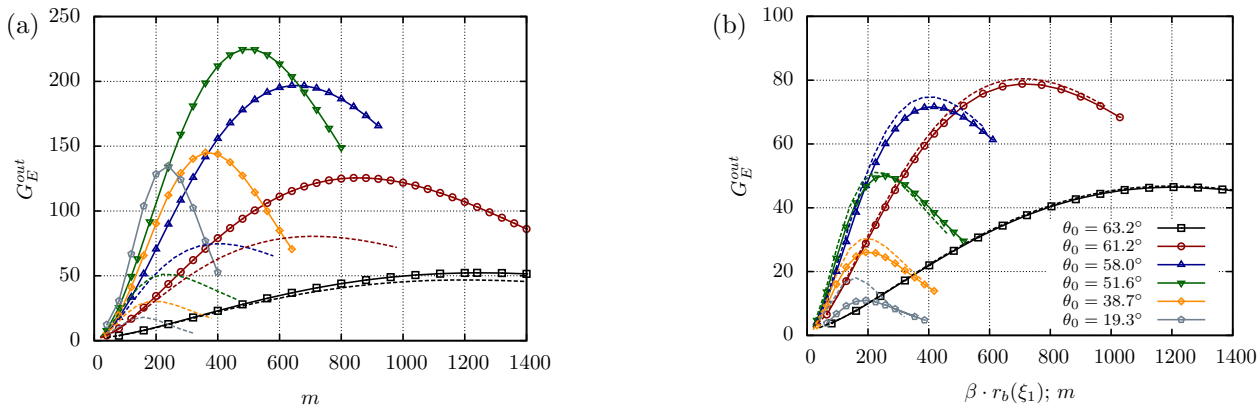

FIG. 9. Optimal outlet energy gain G_E^{out} as a function of the azimuthal wavenumber m neglecting (a) streamwise curvature ($h_\xi = 1$) and (b) azimuthal curvature ($h_\zeta = 1$) effects for selected initial positions and same final position, $\theta_1 = 64.5°$. For reference, results accounting for both curvatures are added as dashed lines with the corresponding colors. Note that both subfigures share the same legend.

increases the maximum energy amplification by a factor of approximately 3.

Results analogous to those in Figs. 6(b) and 6(c) but based on the alternate definition of objective function corresponding to the mean energy gain are shown in Figs. 10(a) and 10(b), respectively. By optimizing the mean energy gain over the streamwise domain, the results in Fig. 10 account for the interior maximum in disturbance energy observed with the conventional, outlet energy gain (Fig. 8). Figure 10(a) shows an important disparity between both energy gain definitions for $\theta_1 = 64.5°$. While the optimal outlet energy gain decreases as the inflow location moves closer to the stagnation point, the optimal mean energy gain has a local minimum for $\theta_0 \approx 45°$ and continues to increase for $\theta_0 \to 0$. The optimal azimuthal wavenumbers are consistently larger for the mean energy gain optimization at each initial location. Results of Fig. 10(a) for G_E^{mean} and $\theta_1 = 64.5°$ resemble those of Fig. 6(c) for G_E^{out} and $\theta_1 = 32.2°$, because the mean energy gain definition accounts for the nonmonotonic evolution of $E(\xi)$, which as will be shown next, reaches its maxima within the optimization domain and close to $\theta \approx 30°$ for $\theta_0 = 12.9°$ and $\theta_0 = 19.3°$. Figure 10(b) shows the effect of initial location on the optimal gain for the final optimization location $\theta_1 = 32.2°$. The differences between the results with both energy gain definitions are less noticeable for this case. The initial and final disturbance amplitude vectors corresponding to $\theta_1 = 32.2°$ are plotted in Fig. 11 for two combinations of initial locations and optimal azimuthal wavenum-

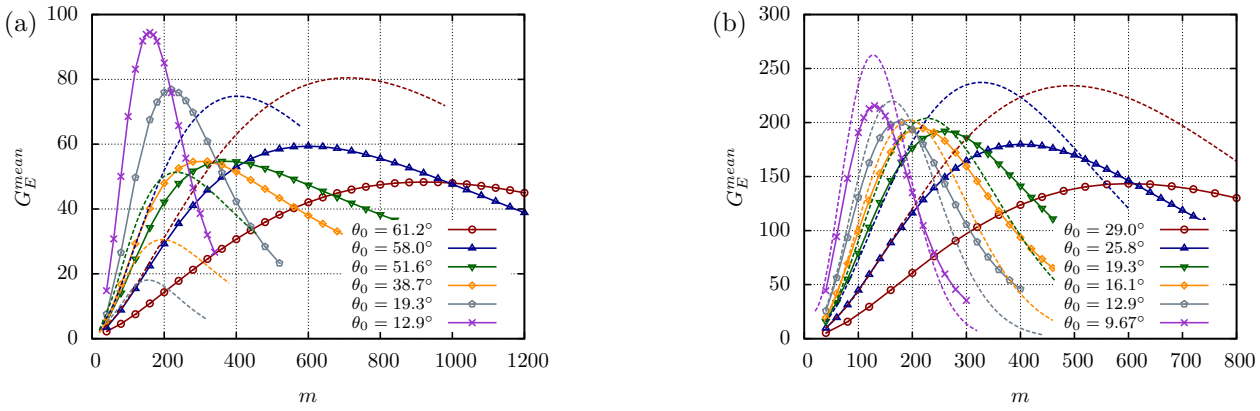

FIG. 10. Optimal mean energy gain G_E^{mean} as a function of the azimuthal wavenumber m for selected initial and final optimization positions (a) $\theta_1 = 64.5°$ and (b) $\theta_1 = 32.2°$. The results with $J = G_E^{out}$ are added for reference as dashed lines with the corresponding colors for each θ_0.

bers. Specifically, Fig. 11(a) corresponds to $\theta_0 = 9.67°$ and $m = 130$ whereas Fig. 11(b) corresponds to $\theta_0 = 25.8°$ and $m = 400$. The optimal initial perturbations based on the two different objective functions are compared with each other for the fixed set of parameters corresponding to $\theta_0 = 9.67°$, $\theta_1 = 32.2°$, and $m = 130$. Between the initial profiles corresponding to mean energy gain (Fig. 11(a)) and those based on the outlet energy gain, the mean energy gain corresponds to wall-normal and azimuthal velocity profiles with a shorter wall-normal extension and the peaks of these profiles are located closer to the wall. Specifically, the peak of the wall-normal velocity moves closer to the wall by a factor of approximately 4. Thereby, the choice of objective function based on the mean energy gain appears more relevant to roughness-induced perturbation. The final perturbations are rather similar for both objective functions. Analogous comparison for the shorter optimization interval of $\theta_0 = 25.8°$ and $\theta_0 = 32.2°$ can be made on the basis of results for mean energy gain with $m = 400$ in Fig. 11(b) and those for outlet energy gain with $m = 320$ in Fig. 7(b). In this case, both initial and final perturbation profiles are similar for both definitions of the energy gain, although the peak of the wall-normal velocity is again located closer to the wall due to the combined effect of choosing mean energy gain as the metric for optimization and the larger azimuthal wavenumber corresponding to the maximum gain in this case.

The streamwise evolution of disturbance energy based on the optimization of mean energy gain across the spatial intervals from Fig. 10 (and corresponding optimal azimuthal wavenumbers), is plotted in Fig. 12. For most initial positions of interest, the disturbance

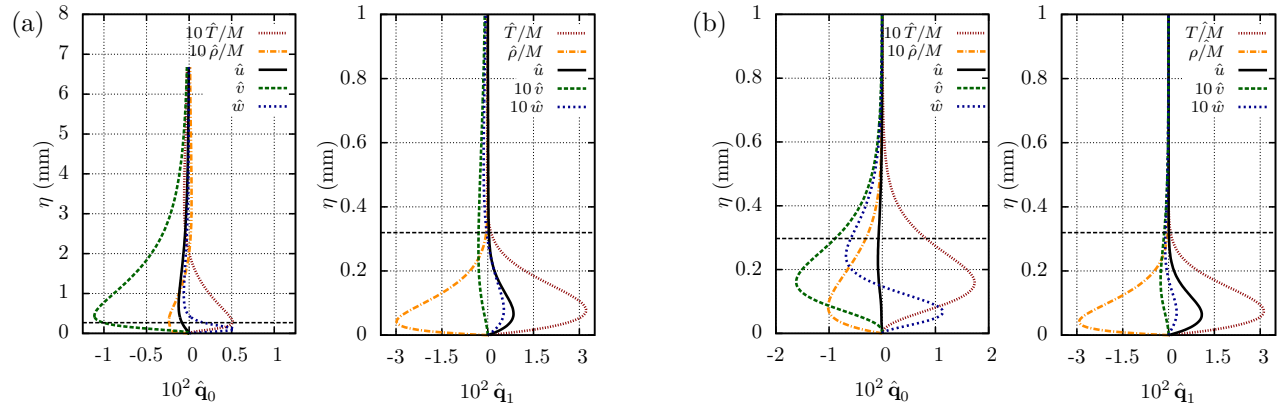

FIG. 11. Initial and final amplitude vectors for optimal mean energy gain G_E^{mean}, $\theta_1 = 32.2°$, (a) $\theta_0 = 9.67°$ and $m = 130$ and (b) $\theta_0 = 25.8°$ and $m = 400$. The profiles are normalized with the local energy norm E. The horizontal dashed lines represent the boundary-layer edge.

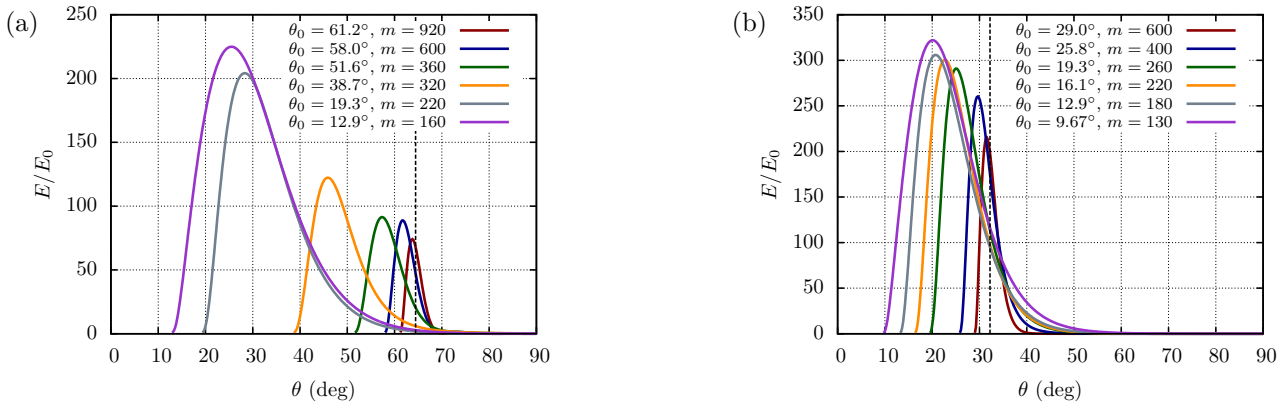

FIG. 12. Evolution of energy norm for highest gain in mean energy for selected initial location for a fixed θ_1: (a) $\theta_1 = 64.5°$ and (b) $\theta_1 = 32.2°$. The plots display energy evolution over the entire length of hemisphere and the fixed value of θ_1 in each case is indicated by the vertical dashed line.

energy obtained in this manner reaches larger values within the optimization domain than those obtained by optimizing the outlet energy gain (Fig. 8).

2. Overall transient growth results

The optimal mean energy gain G_E^{mean} is plotted in Fig. 13(a) in the parameter space of θ_0 and θ_1, for each corresponding optimal azimuthal wavenumber m. The domain of the contour plot is limited by the line $\theta_1 = \theta_0$ (i.e., zero optimization interval or $G_E = 0$) on the bottom and by the line $\theta_1 >> \theta_0$ (i.e., rather larger optimization interval) on the top.

The region beyond the upper boundary is excluded herein because the initial perturbation profiles (particularly the wall-normal velocity) for these parameter values do not exhibit sufficient decay at the wall-normal distance corresponding to the shock location and the transient growth analysis is not able to converge to a satisfactory result. Therefore, this portion of the plot is deemed unnecessary for the present analysis because the perturbations with an extended wall-normal support are unlikely to be excited by wall roughness. Figure 13(a) confirms the previous observations based on the energy norm E from Eq. (8). The highest energy gain occurs for relatively short optimization intervals in the vicinity of the stagnation point as indicated by the black line nearly parallel to the lower boundary of the plot. Figure 13(b) shows the evolution of the energy norm E for parameters that produce the maximum mean energy gain at selected θ_0. The maximum energy ratio is $E/E_0 \approx 500$. The evolution of the kinetic energy budget for these perturbations is also shown in this plot. Compared to the total energy norm E of Eq. (8), the kinetic energy norm K of Eq. (10) exhibits a different trend as seen from Fig. 13(b). The kinetic energy growth for optimal perturbations initiated near the stagnation point is negligible compared with the growth in total energy E. Specifically, the maximum kinetic energy ratio for $\theta_0 = 1.91°$ is $K/K_0 \approx 2$. As the initial location is moved downstream, the kinetic energy content of the perturbation increases and for $\theta_0 = 51.0°$, the magnitude of kinetic and total energy norms are nearly equivalent. The stability analysis of finite-amplitude streaks in compressible boundary layers [50, 51], as well as the analysis of Paredes *et al.* [52] for the present configuration, shows that the secondary instabilities that can potentially lead to bypass transition are driven by the strength of the streamwise velocity shear. Therefore, the reduced kinetic energy content of the perturbations initiated near the stagnation point as seen in Fig. 13(b), motivates the alternate selection of the energy norm for optimization, namely, one that is based on the kinetic energy alone.

Figure 14(a) shows iso-contours of optimal mean kinetic energy gain G_K^{mean} in the parameter space of θ_1 and θ_0. Similar to Fig. 13(a), the results are delimited by $\theta_1 = \theta_0$ and $\theta_1 >> \theta_0$. The main difference between both figures is that for optimization of G_K there exists an optimum set of parameters that lead to a maximum G_K^{mean} in the interior of the domain. Also, this interior peak exists only for $\theta_0 > 15°$. Figure 14(b) shows the evolution of the kinetic energy K and total energy E for the selected sets of parameters that produce the maximum gain in mean kinetic energy at selected values of θ_0. A similar

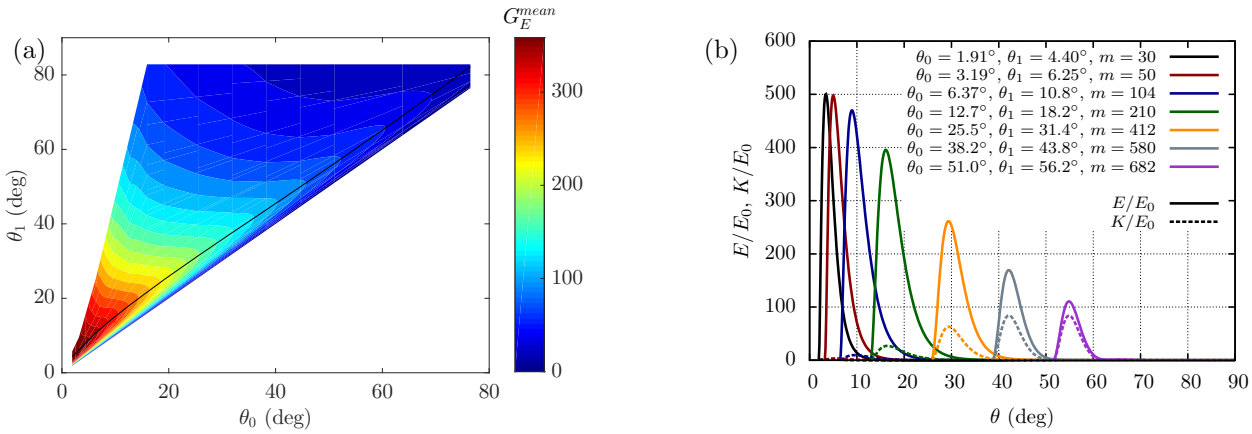

FIG. 13. (a) Contours of optimal mean energy gain G_E^{mean} and (b) evolution of E/E_0 and K/E_0 optimizing for optimal combinations of θ_0, θ_1 and m. The solid line in the contour plot indicates the value of θ_1 corresponding to maximum G_E^{mean} for a given θ_0.

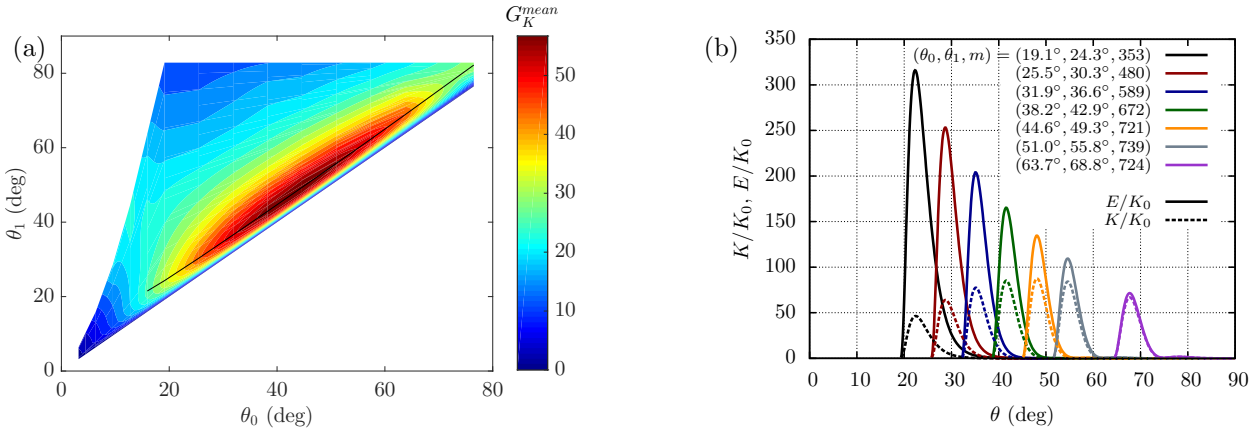

FIG. 14. (a) Contours of optimal mean kinetic energy gain G_K^{mean} and (b) evolution of K/K_0 and E/K_0 for optimal combinations of θ_0, θ_1 and m. The solid line in the contour plot indicates the value of θ_1 corresponding to maximum G_K^{mean} for a given θ_0.

trend to Fig. 13(b) is observed; while the kinetic energy experiences a maximum growth of $K/K_0 \approx 90$ for $\theta_0 \approx 44°$, the total energy growth is reduced for larger θ_0. For the largest θ_0 plotted, $\theta_0 = 63.7°$, the total energy is almost equivalent to the kinetic energy.

The pairs of parameters θ_1 and m that lead to the maximum values of G_E^{mean} and G_K^{mean} for selected θ_0 values are plotted in Fig. 15. As previously observed, G_E^{mean} experiences a monotonic decay from $\theta_0 \approx 2°$ and G_K^{mean} reaches a maximum value for $\theta_0 \approx 44°$. For the farthest downstream initial locations included in the plot, $G_E^{mean} \approx G_K^{mean}$, i.e., nearly all of

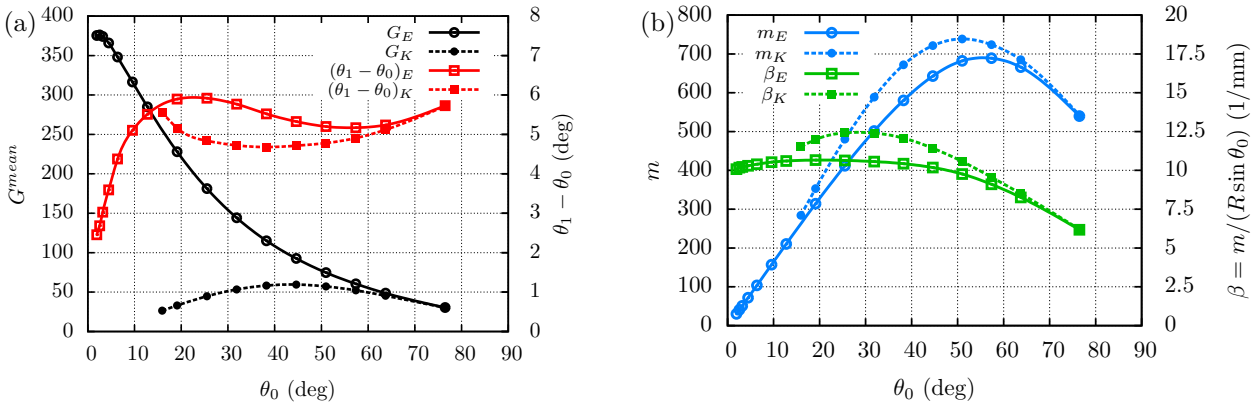

FIG. 15. (a) Optimal mean energy gains, G_E^{mean} and G_K^{mean}, as a function of θ_0 and corresponding optimization intervals, $\theta_1 - \theta_0$, and (b) azimuthal wavenumbers, m, and $\beta = m/(R\sin\theta_0)$.

the overall energy corresponds to the kinetic energy component. Thus, the thermodynamic fluctuations do not experience any growth for those θ_0. Despite the larger values of G_E^{mean} with respect to G_K^{mean}, the kinetic energy contains the streamwise velocity perturbations that lead to secondary instabilities, and subsequently, to the process of laminar breakdown [50–52]. The evolution of G_E^{mean} and G_K^{mean} is rather similar to the evolution of basic state quantities corresponding to the wall normal derivatives of temperature, $\bar{T}_\eta$, and streamwise velocity, $\bar{u}_\eta$, at the wall (Fig. 3(a)). The optimization interval $(\theta_1 - \theta_0)$ that produces the maximum G_E^{mean} and G_K^{mean} falls within the narrow range of $(\theta_1 - \theta_0) \in (5°, 6°)$ for $\theta_0 > 10°$. The short optimization distance is in line with the findings by Theiss *et al.* [74] pertaining to the wakes of isolated roughness element over a spherical forebody. The laminar stationary wake of the roughness element experiences a growth and decay of the streak amplitude within a short distance, equal to just a few roughness-element diameters downstream of the element. The optimal azimuthal wavenumber m and corresponding local spanwise wavenumber $\beta = m/(R\sin(\theta_0))$ are plotted in Fig. 15(b). For initial locations lower than $\theta_0 = 45°$, the optimal azimuthal wavenumber shows a nearly linear trend with θ_0, but the optimal local spanwise wavenumber $\beta = m/(R\sin(\theta_0))$ for optimal G_E and optimal G_K is contained within the narrow ranges of $\beta_E \in (10, 10.7)$ 1/mm and $\beta_K \in (11.5, 12.5)$ 1/mm, respectively.

Next, the transient growth amplification is plotted in terms of the logarithmic amplification ratio, the so-called N-factor, based on the total energy norm N_E, or kinetic energy

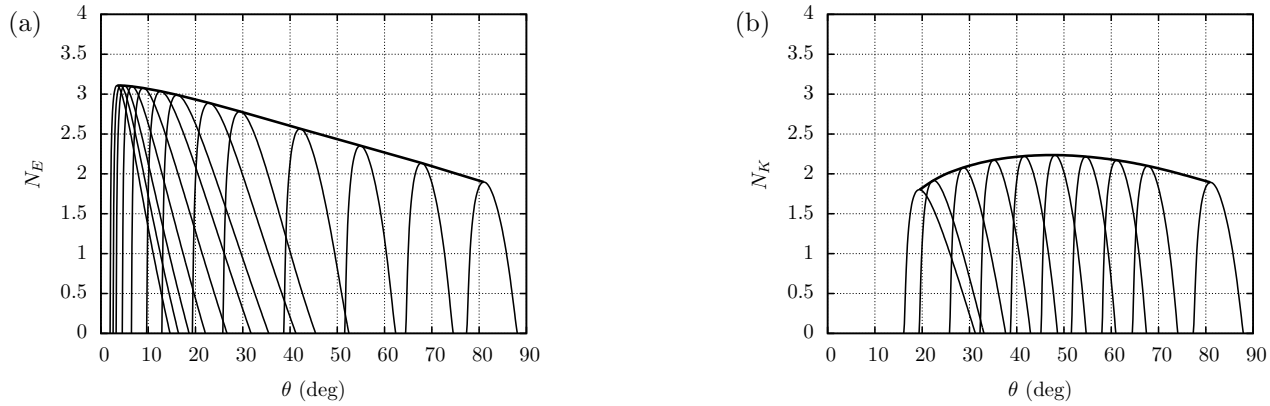

FIG. 16. N-factor curves (thin lines) and envelope (thick line) based on (a) total energy growth N_E (b) kinetic energy growth N_K. The optimal parameters for maximum (a) G_E^{mean} and (b) G_K^{mean} are selected for each θ_0.

norm N_K, defined as

$$N_E(\xi) = 1/2 \ln[E(\xi)/E(\xi_0)], \tag{14}$$

$$N_K(\xi) = 1/2 \ln[K(\xi)/K(\xi_0)]. \tag{15}$$

Figure 16(a) and 16(b) show the N_E curves with optimal parameters for maximum G_E^{mean}, and the N_K curves with optimal parameters for maximum G_K^{mean}, respectively. The envelopes show a similar evolution to the optimal gains G_E^{mean} and G_K^{mean}, in Figs. 15(a). While the maximum N_E occurs close to the stagnation point, the maximum N_K is found at $\theta = 47.5°$.

Figure 17 shows the effect of outflow location θ_1 and azimuthal wavenumber m on the evolution of the disturbance kinetic energy along the hemisphere, i.e., $\theta = [\theta_0, 90°]$, for a fixed initial position of $\theta_0 = 44.7°$ that approximately corresponds to the optimal initial location for the highest overall gain in mean kinetic energy. For increasing θ_1, the corresponding optimal m decreases, compounding the increase in streak spacing because of increased transverse radius at farther downstream locations. The maximum kinetic energy is achieved for the conditions that coincide with those for the maximum mean kinetic energy gain. Figure 17(b) shows the evolution of the kinetic energy at various values of m for a fixed $\theta_1 = 49.3°$. In this plot, only the curve with $m = 721$ corresponds to the optimal wavenumber for the physical interval of interest, namely, $(\theta_0, \theta_1) = (44.7°, 49.3°)$. Increasing values of m are seen to reduce the streamwise length of the region over the disturbance kinetic energy would exceed a specified threshold.

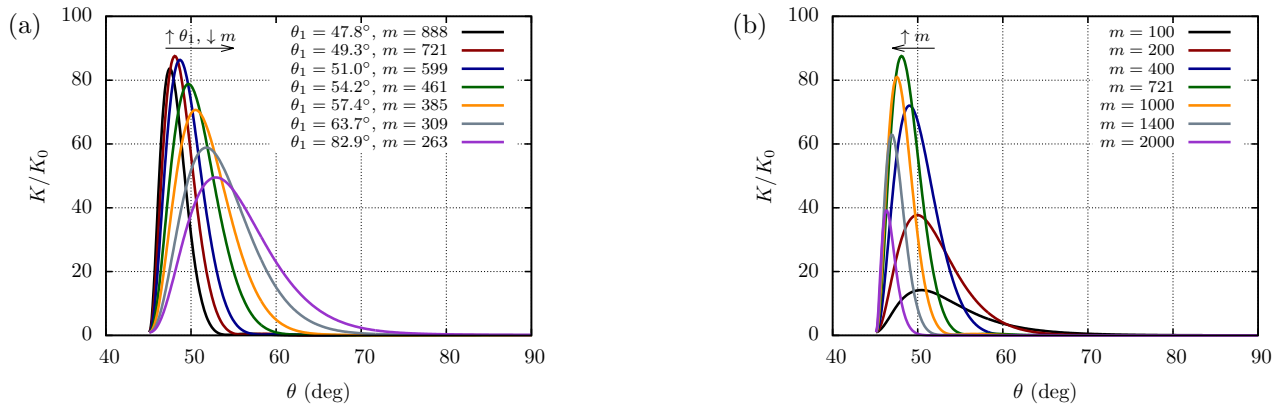

FIG. 17. Effect of final optimization location θ_1 and azimuthal wavenumber m on kinetic energy evolution for optimal mean kinetic energy gain G_K^{mean} and $\theta_0 = 44.6°$. Subfigure (a) shows evolution of optimal perturbations with combinations of θ_1 and m, and subfigure (b) shows evolution of optimal perturbations with suboptimal selected m with fixed $\theta_1 = 49.3°$.

C. Implications of transient growth predictions

Herein, the results of this optimal growth analysis are used to reexamine the highly successful transition criteria of Reshotko and Tumin [36] and the experimental observations of transition near the sonic location of Kaattari [49]. Note that for short optimization intervals, the initial optimal disturbance corresponds to pairs of counter-rotating vortices with similar magnitudes of the wall-normal and spanwise velocity components, and with peak-perturbation locations that are contained withing the boundary layer thickness, as shown in Fig. 11(b). Numerical studies [33, 39, 40, 42, 75, 76] have shown that roughness elements induce similar counter-rotating vortices that can experience transient growth. However, the disturbance induced by roughness elements exhibits a significant streamwise velocity component, which is not present in the theoretically optimal perturbations. Therefore, roughness-induced transient growth is certainly possible, but always suboptimal. Despite the reported low amplification ratios in the present configuration, the growth of transient growth streaks induced by subcritical distributed roughness elements might lead to the onset of non-stationary streak instabilities that induce transition shortly after their onset [52, 74].

As introduced by Reshotko and Tumin [36], the optimal kinetic energy gain can be related to roughness-induced kinetic energy, $K_{in} = \bar{\rho}_k \bar{u}_k^2$, by assuming that the roughness-induced velocities are proportional to the roughness height $\bar{u}_k/\bar{u}_e \propto k/\Theta$, and that $\bar{T}_e/\bar{T}_k = \bar{\rho}_k/\bar{\rho}_e$,

where $\bar{T}_k = \bar{T}_w$. Then, the induced kinetic energy can be written as

$$K_{in} \propto \frac{\bar{T}_e}{\bar{T}_w} \left(\frac{k}{\Theta}\right)^2 \bar{\rho}_e \bar{u}_e^2. \tag{16}$$

Here, $\bar{\rho}_e \bar{u}_e^2$ is not uniform along the streamwise direction (Fig. 2(a)) and therefore, is included in Eq. (16). Note that this term was not included in the correlation derived by Reshotko and Tumin [36], because they performed a local analysis and used the edge boundary layer values for nondimensionalization, while here, the global freestream values are used to be consistent with the transient growth analysis of Subsection III B.

Furthermore, the energy at the transition location is assumed to be

$$K_{tr} = G_K K_{in} \propto G_K^{mean} \frac{\bar{T}_e}{\bar{T}_w} \left(\frac{k}{\Theta}\right)^2 \bar{\rho}_e \bar{u}_e^2. \tag{17}$$

Finally, in the spirit of an absolute amplitude criterion for transition, the transition onset location is associated with a critical disturbance amplitude $A_{tr} = \sqrt{K_{tr}} \propto c_k k$, where c_k is defined as the roughness-induced transfer function from roughness height to amplitude disturbance,

$$c_k = \sqrt{\left(G_K^{mean} \frac{\bar{T}_e}{\bar{T}_w} \bar{\rho}_e\right)} \frac{\bar{u}_e}{\Theta}. \tag{18}$$

This critical disturbance amplitude is assumed to corresponds to the amplitude required for sufficient amplification of secondary instabilities to achieve subsequent breakdown. At the location of maximum c_k ($\theta_{c_{k,max}}$), the roughness height required to produce a certain disturbance amplitude is minimum, i.e., $\theta_{c_{k,max}} = \theta_{k_{min}}$, and $k \propto 1/c_k$. Eq. 18 can be related to the correlation of Eq. 3 derived by Reshotko and Tumin [36], by dropping ρ_e and u_e because of the local assumption used in their analysis and by assuming $G^{1/2}/Re_\Theta \propto (2T_w/T_e)^{-0.77}$.

The optimal mean kinetic energy gain (previously plotted in Fig. 15(a)) divided by its maximum value, $G_{K,max} = 59.6$, is shown in Fig. 18(a), together with the locations corresponding to the sonic point $M_e = 1$ and maximum wall shear (or equivalently, the maximum of $(\bar{u}_\eta)_w$ for this case with constant wall temperature). The locations for maximum G_K^{mean} and $(\bar{u}_\eta)_w$ are almost at the same downstream position. This result is in agreement with incompressible parallel transient growth theory, where the nonmodal growth is known to be driven by the velocity shear [2]. Figure 18(b) shows that $\theta_{k_{min}} = 39.2°$, which is slightly upstream of the sonic location $\theta_{M_e=1} = 41.1°$. This result is in agreement with the experimental observations of the PANT Program [43, 44], which reported that roughness induced

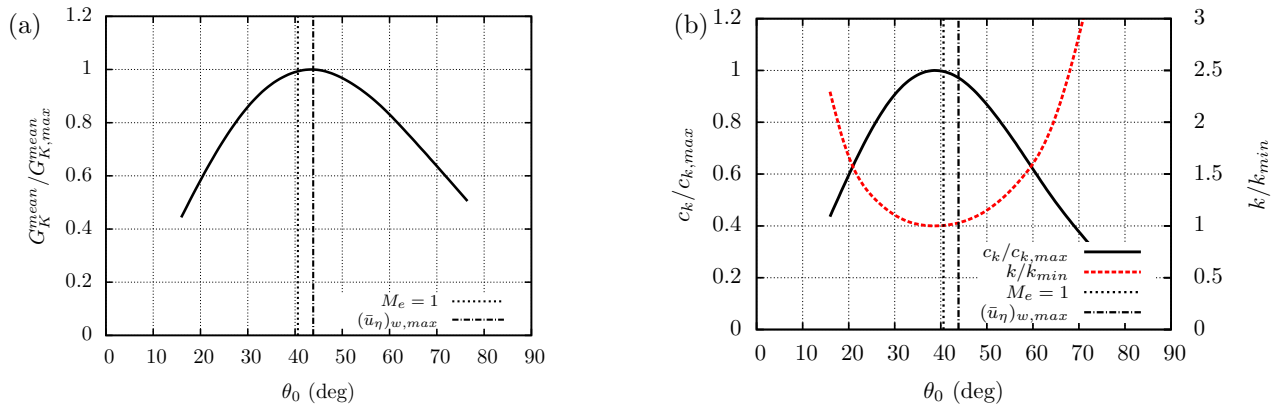

FIG. 18. (a) Optimal mean kinetic energy gain and (b) roughness-induced transfer function and roughness height. The values are normalized with their corresponding maximum or minimum. The vertical lines denote the sonic point and the location for maximum wall shear.

TABLE I. Comparison of angular location of minimum required roughness height for transition onset with predictions by PANT [43, 44], Reda [35] and Reshotko & Tumin (RT) [36] roughness-induced transition correlations.

	PANT	Reda	RT: Parallel, G_E	Nonparallel, G_K^{mean}
$\theta_{k_{min}}$	27.3°	34.8°	36.9°	39.2°

transition flashed upstream from the cone to somewhere ahead of the sonic point when $Re_\Theta \left(\frac{k}{\Theta}\frac{T_e}{T_w}\right)^{0.7} \geq 255$ at the sonic point. Furthermore, Table I shows that the location $\theta_{k_{min}}$ is in agreement with the transition locations predicted by roughness-induced transition correlations. The present geometry and flow conditions correspond to the experiment study of Kaattari [49], who focused on the effects of mass addition on transition and heat transfer. Transition onset was not observed for zero mass injection. As the mass injection rate was increased, the transition location was first observed at $\theta_{tr} \approx 45°$, which is in good agreement with the present prediction, $\theta_{k_{min}} = 39.2°$, taking into account that the optimization interval is approximately 5° (Fig. 15(a)). Note that although the mass injection can be considered as a wall roughness, it also modifies the boundary layer profiles [48] and the analysis presented here is performed for the zero mass addition case in the same way that the roughness correlations are applied using boundary layer parameters evaluated for the no roughness case.

IV. CONCLUDING REMARKS

Optimal transient growth analysis has been conducted for the laminar flow based on the solution of the Navier-Stokes equations over a hemisphere of radius $R = 0.0889$ m at zero angle of attack and freestream conditions corresponding to the experiment of Kaattari [49], namely, $M_\infty = 7.32$, $Re' = 14.6 \times 10^6$ /m, and $T_\infty = 65$ K. The parabolized stability equations (PSE) were used in a variational approach to obtain the optimal initial disturbance that leads to the maximum energy gain for a selected streamwise domain and azimuthal disturbance wavenumber.

A commonly used objective function for optimal growth predictions corresponds to inlet-to-outlet gain in the so called Mack's energy norm, which combines the contributions from both kinetic and thermodynamic fluctuations. For this choice of objective function, the predicted trends based on the Navier-Stokes basic state are in agreement with the previous results [45, 46] based on a local-similarity solution to boundary layer equations; specifically, the transient growth is stronger in the vicinity of the stagnation point and the convex curvature reduces the optimal energy amplification. The results are also consistent with prior predictions for the incompressible, planar Hiemenz flow in that, for optimization domains close to the stagnation point, the optimal azimuthal wavenumber becomes rather small and the initial perturbation profile extends beyond the boundary layer edge [62]. In the present hypersonic case, the optimum initial profile extends into the shock layer, indicating a significant wall-normal velocity perturbation at locations approaching the bow shock. Such perturbations are unlikely to represent roughness-induced transition.

Optimal growth computations are also performed using an alternate objective function that maximizes the mean energy gain over the integration domain. The latter selection of objective function yields larger energy amplification and the resulting optimal initial disturbance profiles move closer to the wall, denoting perturbations that may be more easily realizable via surface roughness. Although the maximum energy gain is obtained for short optimization intervals with initial locations near the stagnation point, the streamwise velocity shear of the basic flow profiles is very small in the vicinity of the stagnation point, and consequently, the optimal perturbations excited near this location do not lead to downstream perturbations with the highest kinetic energy.

The transient growth disturbances are purely stationary and their growth cannot amount

to laminar-turbulent transition. The growth of transient growth streaks can lead to the onset of non-stationary streak instabilities that typically amplify rather rapidly and induce transition shortly after their onset. The growth of streak instabilities is intimately connected with the amplitude of transient growth streaks. Because the streak instabilities are mostly driven by streamwise velocity shear [50–52], a greater content of kinetic energy within a specified total energy is likely to enhance the growth of those instabilities, and therefore, potentially lead to an earlier onset of bypass transition. For this reason, transient growth analysis was performed with the mean kinetic energy gain as the objective function. The results show that the maximum kinetic energy gain is obtained for an initial location approximately coincident with the maximum-wall-shear position, which for the present case is located approximately 3° downstream of the sonic point at $\theta_{M_e=1} = 41.1°$. By assuming that the initial perturbation velocity induced by the roughness is proportional to the roughness height and that the ratio of basic state densities near the boundary layer edge and roughness height, respectively, is proportional to the wall-cooling factor, a transfer function from roughness height to disturbance amplitude is defined and has a maximum at $\theta = 39.2°$. A larger transient growth disturbance amplitude is directly linked to a greater destabilization of the secondary instabilities and subsequent breakdown. This maximum corresponds to the location where a minimum roughness height would be required to produce a certain disturbance amplitude. This position is compared with roughness-induced transition correlations [35, 36, 44] and the agreement is satisfactory. Furthermore, Kaattari [49] measured the transition location for minimum mass injection at $\theta \approx 45°$, which is in good agreement with the predicted location of peak boundary layer perturbation, considering that the length of the optimization interval is approximately 5°.

The implications of these findings for the transition correlation derived by Reshotko and Tumin [36] are not obvious; however, it will be worthwhile to investigate those in future work by using the present theoretical formulation to examine the dependence of transient growth on wall temperature, freestream Mach number, and geometry radius, and then attempting to derive a revised transition criterion based on the stronger foundation of nonparallel spatial transient growth.

The optimal energy gains and corresponding initial profiles vary with the choice of energy norm, and also of the objective function. We show herein that in certain important problems as the blunt-body paradox, the potential utility of the optimal growth theory could

be improved by making judicious selections of energy norm and objective functions. The resulting predictions provide a possible explanation for the experimental observation that roughness induced transition over blunt bodies occurs near or somewhat upstream of the sonic point.

We note that the generation (i.e., receptivity) of the streak disturbances has not been addressed in this paper. As previously mentioned, disturbance profiles resulting from realistic external disturbances result in suboptimal transient growth. The present results based on optimal initial disturbances may therefore be viewed as providing an upper bound on nonmodal energy amplification due to spanwise periodic disturbances.

The results show a maximum logarithmic amplification ratio based on kinetic energy norm of $N_K = 2.24$, which corresponds to an amplitude growth of $A/A_0 = \sqrt{K/K_0} \approx 10$. Paredes *et al.* [52] show that the present boundary layer perturbed by finite-amplitude optimal perturbations becomes unstable for streak amplitudes $As_u > 0.16$. Therefore, the needed initial amplitudes of optimal perturbations for secondary instability would be $A_0 > 0.01$. Taking into account that perturbations induced by distributed roughness are suboptimal [40], a realistic perturbation would need even larger initial amplitudes. Consequently, nonlinear effects are expected to be important and, therefore, the study of suboptimal nonlinear perturbations that are more readily realizable via distributed roughness would be very helpful. We hope that the present set of results would spur analyses of this type and also provide useful guidance for defining the relevant roughness configurations.

ACKNOWLEDGMENTS

This research was sponsored by the NASA Transformational Tools and Technologies (TTT) Project of the Transformative Aeronautics Concepts Program under the Aeronautics Research Mission Directorate. A portion of the computational resources supporting this work were provided by the NASA High-End Computing (HEC) Program through the NASA Advanced Supercomputing (NAS) Division at Ames Research Center.

---

[1] L.M. Mack, "Boundary layer linear stability theory," in *AGARD–R–709 Special course on stability and transition of laminar flow* (1984) pp. 3.1–3.81.

[2] P.J. Schmid and D. S. Henningson, *Stability and Transition in Shear Flows* (Springer, New York, 2001).

[3] W.S. Saric and A.H. Nayfeh, "Nonparallel stability of boundary-layer flow," Phys. Fluids **18**, 945–950 (1975).

[4] T. Herbert, "Parabolized stability equations," Ann. Rev. Fluid Mech. **29**, 245–283 (1997).

[5] F.P. Bertolotti, T. Herbert, and P.R. Spalart, "Linear and nonlinear stability of the Blasius boundary layer," J. Fluid Mech. **242**, 441–474 (1992).

[6] K.M. Case, "Stability of plane Couette flow," Phys. Fluids **3**, 143–148 (1960).

[7] J.T. Stuart, "The production on intense shear layers by vortex stretching and convection," NATO AGARD Report No. 514. (also: National Phys. Lab. Aeronaut. Res. Rep. 1147) (1965).

[8] M.T. Landahl, "A note on algebraic instability of inviscid parallel shear flows," J. Fluid Mech. **98**, 243–251 (1980).

[9] P.J. Schmid, "Nonmodal stability theory," Annu. Rev. Fluid Mech. **39**, 129–162 (2007).

[10] E. Reshotko, "Transient growth: A factor in bypass transition," Phys. Fluids **13**, 1067–1075 (2001).

[11] M.V. Morkovin, "On the many faces of transition," in *Viscous Drag Reduction: Proceedings of the Symposium on Viscous Drag Reduction held at the LTV Research Center, Dallas, Texas, September 24 and 25, 1968*, edited by C. Sinclair Wells (Springer US, Boston, MA, 1969) pp. 1–31.

[12] M.V. Morkovin, E. Reshotko, and T. Herbert, "Transition in open flow systems - A reassessment," Bull. Am. Phys. Soc. **39**, 1882 (1994).

[13] E. Reshotko, "Boundary layer transition, instability and control," AIAA Paper 94-0001 (1994).

[14] E. Reshotko and A. Tumin, "Spatial theory of optimal disturbances in a circular pipe flow," Phys. Fluids **13**, 991–996 (2001).

[15] K. Avila, D. Moxey, A. De Lozar, M. Avila, D. Barkely, and B. Hof, "The onset of turbulence in pipe flow," Science **333**, 192–196 (2011).

[16] D. Barkley, "Theoretical perspective on the route to turbulence in a pipe," J. Fluid Mech. **803**, P1–1–80 (2016).

[17] E. Reshotko, "Preliminary experimental study of disturbances in a laminar boundary layer due to distributed surface roughness," AIAA Paper 81-1224 (1981).

[18] E.B. White, "Transient growth of stationary disturbances in a flat plate boundary layer,"

Phys. Fluids **14**, 4429–4439 (2002).

[19] N.S. Sharp and E.B. White, "Roughness-induced transient growth on a hypersonic blunt cone," AIAA Paper 2014-0432 (2014).

[20] J.D. Murphy and M.W. Rubesin, "Re-evaluation of heat-transfer data obtained in flight test of heat-sink shielded re-entry vehicles," J. Spacecraft **3**, 53–60 (1966).

[21] E. Reshotko and A. Tumin, "The blunt body paradox - A case for transient growth," in *Proc. of the IUTAM Laminar-Turbulent Symposium V*, edited by H. Fasel and W. Saric (Sedona, AZ, USA, 2000) pp. 403–408.

[22] S.P. Schneider, "Hypersonic boundary-layer transition on blunt bodies with roughness," AIAA Paper 2008-0501 (2008).

[23] B.R. Hollis, "Blunt-body entry vehicle aerothermodynamics: transition and turbulence on the CEV and MSL configurations," AIAA Paper 2010-4984 (2010).

[24] B.R. Hollis, "Blunt-body entry vehicle aerothermodynamics: transition and turbulent heating," J. Spacecraft Rockets **49**, 435–449 (2012).

[25] A. Theiss, S. Hein, D. Heitmann, S.R.C. Ali, and R. Radespiel, "Numerical and experimental investigation of laminar-turbulent boundary layer transition on a blunt generic re-entry capsule," AIAA Paper 2014-2353 (2014).

[26] A.N. Leidy, E. Reshotko, F. Siddiqui, and R.D.W. Bowersox, "Characterizing the transient growth mechanism on a hypersonic blunt body at a high angle of attack," AIAA Paper 2016-3951 (2016).

[27] B.R. Hollis and D.S. Liechty, "Transition due to heat-shield cavities on a Mars Entry Vehicle," J. Spacecraft Rockets **43**, 354–366 (2006).

[28] D.C. Reda, "Transition experiments on blunt bodies with distributed roughness in hypersonic free flight," J. Spacecraft Rockets **45**, 210–215 (2008).

[29] B. Wheaton and S. Schneider, "Roughness-induced instability in a hypersonic laminar boundary layer," AIAA J. **5**, 1245–1256 (2012).

[30] P.S. Iyer and K. Mahesh, "High-speed boundary-layer transition induced by a discrete roughness element," J. Fluid Mech. **729**, 524–562 (2013).

[31] P.K. Subbareddy, M.D. Bartkowicz, and G.V. Candler, "Direct numerical simulation of high-speed transition due to an isolated roughness element," J. Fluid Mech. **748**, 848–878 (2014).

[32] J.-C. Loiseau, J.-C. Robinet, S. Cherubini, and E. Leriche, "Invistigation of the roughness-

induced transition: global stability analyses and direct numerical simulations," J. Fluid Mech. **760**, 175–211 (2014).

[33] G. Groskopf and M.J. Kloker, "Instability and transition mechanisms induced by skewed roughness elements in a high-speed laminar boundary layer," J. Fluid Mech. **805**, 262–302 (2016).

[34] D.C. Reda and R.A. Leverance, "Boundary-layer transition experiments on pre-ablated graphite nosetips in a hyperballistics range," NSWC-WOL-TR-76-71, Naval Surface Weapons Center, White Oak Laboratory (1975).

[35] D.C. Reda, "Correlation of nosetip boundary-layer transition data measured in ballistic range experiments," AIAA J. **19**, 329–339 (1981).

[36] E. Reshotko and A. Tumin, "Role of transient growth in roughness-induced transition," AIAA J. **42**, 766–770 (2004).

[37] J.H.M. Fransson, L. Brandt, A. Talamelli, and C. Cossu, "Experimental and theoretical investigation of the non-modal growth of steady streaks in a flat plate boundary layer," Phys. Fluids **16**, 3627–3638 (2004).

[38] E.B. White, J.M. Rice, and F.G. Ergin, "Receptivity of statoinary transient disturbances to surface roughness," Phys. Fluids **17**, 064109–1–12 (2005).

[39] P. Fischer and M. Choudhari, "Numerical simulation of roughness-induced transient growth in a laminar boundary layer," AIAA Paper 2004-2539 (2004).

[40] M. Choudhari and P. Fischer, "Roughness induced transient growth," AIAA Paper 2005-4765 (2005).

[41] J.H.M. Fransson and A. Talamelli, "On the generation of steady streamwise streaks in flat-plate boundary layers," J. Fluid Mech. **698**, 211–234 (2012).

[42] M.E. Goldstein, A. Sescu, P.W. Duck, and M. Choudhari, "Nonlinear wakes behind a row of elongated roughness elements," J. Fluid Mech. **796**, 516–557 (2016).

[43] M.J. Abbett, A.D. Anderson, L. Cooper, T.J. Dahm, and J. Kelly, "Passive Nosetip Technology (PANT) Program. Volume 20. Investigation of flow phenomena over reentry vehicle nosetips," SAMSO-TR-74-86, Aerotherm Division/Acurex Corp., Report 75-164 (1975).

[44] M.R. Wool, "Final summary report Passive Nosetip Technology (PANT) Program," SAMSO-TR-75-250, Aerotherm Division/Acurex Corp., Report 75-159 (1975).

[45] A. Tumin and E. Reshotko, "Optimal disturbances in the boundary layer over a sphere,"

AIAA Paper 2004-2241 (2004).

[46] S. Zuccher, A. Tumin, and E. Reshotko, "Parabolic approach to optimal perturbations in compressible boundary layers," J. Fluid Mech. **556**, 189–216 (2006).

[47] L. M. Mack, *Boundary Layer Stability Theory*, Tech. Rep. JPL Rept. 900-277 (California Institute of Technology, Pasadena, CA, 1969).

[48] F. Li, M. Choudhari, C.-L. Chang, and J. White, "Effects of injection on the instability of boundary layers over hypersonic configurations," Phys. Fluids **25**, 104107–1–15 (2013).

[49] G. Kaattari, "Effects of mass addition on blunt-body boundary-layer transition and heat transfer," NASA TP-1139 (1978).

[50] P. Paredes, M.M. Choudhari, and F. Li, "Nonlinear transient growth and boundary layer transition," AIAA Paper 2016-3956 (2016).

[51] P. Paredes, M.M. Choudhari, and F. Li, "Transition due to streamwise streaks in a supersonic flat plate boundary layer," Phys. Rev. Fluids **1**, 083601–1–23 (2016).

[52] P. Paredes, M.M. Choudhari, and F. Li, "Transient growth and streak instabilities on a hypersonic blunt body," AIAA Paper 2017-0066 (2017).

[53] S.J. Leib, D.W. Wundrow, and M.E. Goldstein, "Effect of free-stream turbulence and other vortical disturbances on a laminar boundary layer," J. Fluid Mech. **380**, 169–203 (1999).

[54] M.E. Goldstein, A. Sescu, P.W. Duck, and M. Choudhari, "Algebraic/transcendental disturbance growth behind a row of roughness elements," J. Fluid Mech. **668**, 236–266 (2011).

[55] J.O. Pralits, C. Airiau, A. Hanifi, and D.S. Henningson, "Sensitivity analysis using adjoint parabolized stability equations for compressible flows," Flow Turbul. Combust. **65**, 183–210 (2000).

[56] D. Tempelmann, A. Hanifi, and D.S. Henningson, "Spatial optimal growth in three-dimensoinal boundary layers," J. Fluid Mech. **646**, 5–37 (2010).

[57] D. Tempelmann, A. Hanifi, and D.S. Henningson, "Spatial optimal growth in three-dimensoinal compressible boundary layers," J. Fluid Mech. **704**, 251–279 (2012).

[58] P. Paredes, M.M. Choudhari, F. Li, and C.-L. Chang, "Optimal growth in hypersonic boundary layers," AIAA J. **54**, 3050–3061 (2016).

[59] P. Andersson, M. Berggren, and D.S. Henningson, "Optimal disturbances and bypass transition in boundary layers," Phys. Fluids **11**, 134–150 (1999).

[60] P. Luchini, "Reynolds-number-independent instability of the boundary layer over a flat surface:

Optimal perturbations," J. Fluid Mech. **404**, 289–309 (2000).

[61] A. Tumin and E. Reshotko, "Optimal disturbances in compressible boundary layers," AIAA J. **41**, 2357–2363 (2003).

[62] P. Paredes, M.M. Choudhari, F. Li, and C.-L. Chang, "Transient growth analysis of compressible boundary layers with Parabolized Stability Equations," AIAA Paper 2016-0051 (2016).

[63] F. Li and M.R. Malik, "Mathematical nature of parabolized stability equations," R. Kobayashi (Ed.), Laminar-Turbulent Transition, Springer , 205–212 (1994).

[64] F. Li and M.R. Malik, "On the nature of the PSE approximation," Theor. Comp. Fluid Dyn. **8**, 253–273 (1996).

[65] F. Li and M.R. Malik, "Spectral analysis of parabolized stability equations," Compt. Fluids **26**, 279–297 (1997).

[66] H. Haj-Hariri, "Characteristics analysis of the parabolized stability equations," Stud. Appl. Math. **92**, 41–53 (1994).

[67] S. Bagheri and A. Hanifi, "The stabilizing effect of streaks on Tollmien-Schlichting and oblique waves: a parametric study," Phys. Fluids **19**, 078103–1–4 (2007).

[68] A. Hanifi, P.J. Schmid, and D.S. Henningson, "Transient growth in compressible boundary layer flow," Phys. Fluids **8**, 51–65 (1996).

[69] M. Hermanns and J.A. Hernández, "Stable high-order finite-difference methods based on non-uniform grid point distributions," Int. J. Numer. Meth. Fluids **56**, 233–255 (2008).

[70] P. Paredes, M. Hermanns, S. Le Clainche, and V. Theofilis, "Order 10^4 speedup in global linear instability analysis using matrix formation," Comput. Meth. Appl. Mech. Eng. **253**, 287–304 (2013).

[71] D.K. Litton, J.R. Edwards, and J.A. White, "Algorithmic enhancements to the VULCAN Navier-Stokes solver," AIAA Paper 2003-3979 (2003).

[72] D.C. Reda, "Review and synthesis of roughness-dominated transition correlations for reentry applications," J. Spacecraft Rockets **39**, 161–167 (2002).

[73] C.-L. Chang, M.R. Malik, and M.Y. Hussaini, "Effects of shock on the stability of hypersonic boundary layers," AIAA Paper 90-1448 (1990).

[74] A. Theiss, S. Hein, S.R.C. Ali, and R. Radespiel, "Wake flow instability studies behind discrete roughness elements on a generic re-entry capsule," AIAA Paper 2016-4382 (2016).

[75] N. De Tullio, P. Paredes, N.D. Sandham, and V. Theofilis, "Laminar-turbulent transition

induced by a discrete roughness element in a supersonic boundary layer," J. Fluid Mech. **735**, 613–646 (2013).

[76] N. De Tullio and N.D. Sandham, "Influence of boundary-layer disturbances on the instability of a roughness wake in a high-speed boundary layer," J. Fluid Mech. **763**, 136–165 (2015).